Applied Energy 401 (2025) 126678

Contents lists available at ScienceDirect

Applied Energy

journal homepage: www.elsevier.com/locate/apenergy

A comprehensive system simulation from PEMFC stack to fuel cell vehicle☆

Zhuo Zhang, Sai-Jie Cai, Jun-Hong Cheng, Hao-Bo Guo, Wen-Quan Tao *

Key Laboratory of Thermo-Fluid Science & Engineering of MOE Xi'an Jiaotong University, Xi'an, Shaanxi 710049, PR China

HIGHLIGHTS

- A hierarchical approach from the fuel cell stack to FCV is established.
- Key operating conditions are determined and optimized using ANOVA/GA algorithms.
- The performance variation with operating conditions is predicted by GPR model.
- The proposed EMS can reduce hydrogen use and smooth PEMFC load fluctuations.

GRAPHICAL ABSTRACT

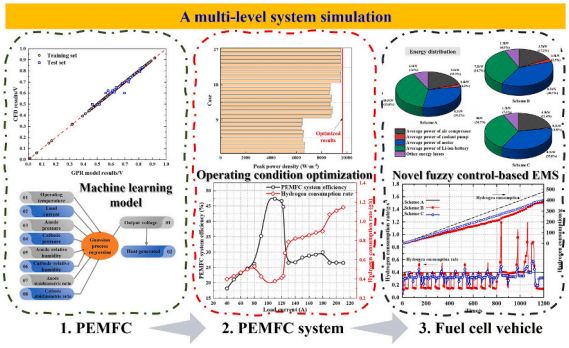

ARTICLE INFO

Keywords:
PEMFC
System simulation
Fuel cell vehicle
Dynamics
Fuel economy

ABSTRACT

The commercialization of fuel cell vehicles (FCVs) is a key method for achieving deep decarbonization in the transportation sector. Boosting powertrain energy conversion and utilization efficiency, especially for fuel cells, is crucial for advancing FCV technology. In the present study, a multi-level FCV system model is developed, and optimization has been carried out at various scales. The results reveal that the Gaussian process regression (GPR) model outperforms other machine learning models in performance prediction accuracy and speed. Then, based on the GPR model, different optimization algorithms are adopted to obtain the optimal operating conditions. Under the hydrogen recirculation architecture of this study, the system efficiency reaches its peak (47.4 %) at a load current of 110 A, which corresponds to the lowest point of hydrogen consumption. By coupling machine learning stack performance prediction models, the dynamic performance and fuel economy of FCVs under the New European Driving Cycle are studied. A novel fuzzy control-based energy management strategy (EMS) is proposed, which can significantly improve energy utilization efficiency while reducing the fuel cell power

Abbreviations: ANOVA, analysis of variance; ANN, artificial natural network; DC, direct current; EMS, energy management strategy; ES, extremely small; EUDC, Extra Urban Driving Cycles; FCV, fuel cell vehicle; FMU, Functional Mock-up Unit; GA, genetic algorithm; GPR, Gaussian process regression; ICE, internal combustion engine; LR, linear regression; MAE, mean absolute error; MEA, membrane electrode assembly; ML, machine learning; MOO, multi-objective optimization; MPC, model predictive control; NEDC, New European Driving Cycle; NTU, number of heat transfer units; PS, pattern search; PEMFC, proton exchange membrane fuel cell; PID, Proportional-Integral-Derivative; PSO, particle swarm optimization; *RMSE*, root mean squared error; R^2, squared correlation coefficient; SAFA, sliding average filtering algorithm; SVR, support vector regression; SOC, state of charge; UDC, Urban Driving Cycles.

☆ This article is part of a Special issue entitled: 'Hydrogen and Smart Cities(Dr. Ren)' published in Applied Energy.

* Corresponding author.
E-mail address: wqtao@mail.xjtu.edu.cn (W.-Q. Tao).

https://doi.org/10.1016/j.apenergy.2025.126678
Received 19 May 2025; Received in revised form 23 July 2025; Accepted 20 August 2025
Available online 2 September 2025

fluctuations. The multi-level optimization research conducted in this article, from the cell itself to the system and then to FCVs, can be widely applied to the design or control of FCVs' powertrain.

Nomenclature

Latin symbols

A	area(m^2)
a	acceleration($m{\cdot}s^{-2}$)
a_w	water activity
C	battery capacity(Ah)
C_d	wind resistance coefficient
C_q	discharge coefficient
c_p	isobaric specific heat capacity($J{\cdot}kg^{-1}{\cdot}K^{-1}$)
c_{vapor}	vapor concentration($mol{\cdot}m^{-3}$)
D	diffusion coefficient($m^2{\cdot}s^{-1}$), diameter(mm)
dh	motor heat loss power(W)
dm	mass flow rate($kg{\cdot}s^{-1}$)
dm_ih_i	the enthalpy flow rate at port i(W)
E_{rev}	reversible voltage(V)
ER	entrainment ratio
F_w	air resistance(N)
F_i	slope resistance(N)
F_f	rolling resistance(N)
F_t	traction force(N)
f	vehicle roll resistance coefficient
h	specific enthalpy($J{\cdot}kg^{-1}$)
h_d	hydraulic diameter(m)
I	load current(A)
k	heat transfer coefficient($W{\cdot}m^{-2}{\cdot}K^{-1}$)
M	equivalent mass or molar mass($kg{\cdot}mol^{-1}$), mass(kg)
m	mass flow rate($kg{\cdot}s^{-1}$)
N	speed ($rev{\cdot}min^{-1}$), number of cells, number of data in the sliding window
Nu	Nusselt number
Pr	Prandtl number
P_{fc}	battery power(kW)
P_r	pressure ratio
P_{fc}	fuel cell output power(kW)
P_m	motor demand power(kW)
P_{oe}	fuel cell output power corresponding to the system efficiency peak(kW)
p	pressure(Pa)
q_m	mass flow rates($kg{\cdot}s^{-1}$)
Q	heat exchange rate(W), flow rate($m3{\cdot}s^{-1}$)
R	thermal resistances($K{\cdot}W^{-1}$), radius(m)
Re	Reynolds number
RH	reletive humidity
St	stoichiometric ratio
$sign$	sign function
T	temperature(K)
T_b	braking torque(N·m)
T_M	driving torque(N·m)
$Torque$	motor torque(N·m)
t	sampling time(s)
U	voltage(V)
V	chamber volume(m^3)
v	vehicle speed($m{\cdot}s^{-1}$)
w	speed ($rev{\cdot}min^{-1}$ or $rad{\cdot}s^{-1}$)
x,x^*	input or output data
Y	mass fraction

Greek letters

Φ	heat transfer rate(W)
ε	efficiency
σ	variance value of data
λ	auxiliary coefficient, membrane water content
α	isobaric thermal expansion coefficient(K^{-1}), slope angle
β_T	isothermal bulk modulus(Pa)
μ	kinetic viscosity(Pa·s), the average value of data
ν	specific volume($m^3{\cdot}kg^{-1}$)
δ	thickness(m)
τ	time constant(s)
ρ	density($kg{\cdot}m^{-3}$)
η	compressor isentropic efficiency
ν_{cr}	critical pressure ratio
γ	isentropic exponent
Δp	pressure drop(Pa)

Subscripts and superscripts

a	anode
ave	average
c	cathode, corrected
compressor	compressor
crit	critical
diff	diffusion
dis	drainage
down	downstream
f	fluid
in	inlet
mem	membrane
pump	pump
sat	saturation
st	reference
T	time T
up	upstream
w	wall
0	stagnation parameter
1	dry
2	outlet parameter, wet

1. Introduction

1.1. Motivations

Hydrogen energy has emerged as a critical part of global decarbonization strategies, offering a versatile solution to mitigate greenhouse gas emissions across hard-to-abate sectors [1], as shown in Fig. 1. In the industrial sector, hydrogen enables the decarbonization of historically carbon-intensive processes. For instance, hydrogen-based direct reduced iron technology can reduce CO_2 emissions in steelmaking by 90 % compared to conventional blast furnaces, addressing an industry responsible for 7 % of global emissions [2]. Hydrogen's role in energy system integration further underscores its importance. By converting surplus renewable electricity into hydrogen via electrolyzers (e.g., proton exchange membrane systems with >75 % efficiency [3]), it provides seasonal energy storage, critical for balancing supply-demand

mismatches in grids dominated by intermittent solar and wind power. In addition to energy storage and industrial applications, with the rapid development of electric vehicles, fuel cell vehicles (FCVs) are considered a key way to achieve large-scale commercialization of hydrogen energy in cities [4].

In recent years, the techno-economic analysis of FCVs has been widely investigated [5]. Shojaeefard and Raeesi [6] assessed the fuel consumption and emissions of FCVs and internal combustion engines (ICEs) under real driving conditions. The results show that FCVs do not produce emissions during driving, and they exhibit approximately 30 % fewer CO_2 emissions than internal combustion vehicles when considering hydrogen production. Yang et al. [7] found that FCVs using hydrogen from electrolysis by abandoned hydropower and coke oven gas have the best performance among all scenarios when the driving mileage reaches around 75,000 km, and their advantage will become more obvious with increasing driving mileage. Therefore, FCVs are the most promising vehicles to achieve environmental protection [8] and energy-efficient utilization in the future [9].

Currently, FCVs predominantly adopt a hybrid power system configuration of "fuel cell and battery" to meet the power requirements of vehicle power systems. Enhancing the energy conversion and utilization efficiency of the powertrain, with a particular focus on the fuel cell, stands as the key to advancing FCV technology further. The energy utilization efficiency of FCVs is influenced by a multi-level set of factors, requiring in-depth analysis across various domains: from the fuel cell stack itself, to the proton exchange membrane fuel cell (PEMFC) system, and ultimately to the vehicle's energy management strategy. First, the operating conditions of the PEMFC, including current density, must be comprehensively analyzed and optimized to maximize its output performance. Second, given the complex dynamic load conditions that FCVs encounter, the performance fluctuations of the PEMFC caused by load changes need to be meticulously modeled and analyzed in greater detail. Finally, to simultaneously achieve low hydrogen consumption and rapid dynamic response in FCVs, an efficient energy management strategy is essential, which necessitates a thorough analysis of energy flow in a typical FCV system.

1.2. Literature review

1.2.1. Optimization of PEMFC operating conditions

The PEMFC serves as the core component of FCVs, functioning to convert hydrogen's chemical energy into electrical energy. Once the key components of a PEMFC, such as the bipolar plates and membrane electrode assembly (MEA), are selected, the operating conditions must be carefully optimized to maximize cell performance [10]. This optimization aims to achieve the highest possible power density while ensuring long-term stability and efficiency. Much work has been done on optimizing the cell operating conditions [11]. Siddiqa et al. [12] proposed a hybrid model and performed a data-driven analysis of some operating and structural parameters' effects on PEMFC. It was found that the operating temperature has a more significant impact on cell performance than the pressure. Feng et al. [13] optimized the performance of fuel cells with ultra-thin vapor chambers. Under high current density, increasing humidity is beneficial for hydrating the membrane, but too high a humidity may lead to increased saturation of liquid water, producing water flooding and impeding oxygen diffusion. Zhou et al. [14] obtained the optimal operating conditions of the proton exchange membrane fuel cell through a multi-objective optimization (MOO) method. The MOO results indicate that a lower temperature, higher relative humidity, and higher stoichiometric ratio can enhance PEMFC comprehensive performance across a range of specific operating conditions.

The above studies are all aimed at optimizing operating conditions (including temperature, humidity, and stoichiometric ratio) in galvanostatic or potentiostatic mode to achieve maximum output performance. However, for an actual PEMFC system, the load current should also be determined. Then, not only the PEMFC itself but also the auxiliary device should be considered. The optimal operating condition should be determined considering the parasitic power of these devices (including the air compressor and coolant pump). As the current density increases, the parasitic power also increases. The system efficiency, defined by the integration of PEMFC power output, parasitic power consumption, and fuel utilization rate, should be established as a comprehensive criterion to serve as the optimization objective [15,16]. When optimizing the operating conditions of the fuel cell stack, Chen et al. [17] estimated the parasitic power and hydrogen consumption through empirical formulas. However, this method can not accurately consider the working characteristics of real auxiliary machines. Especially on the hydrogen side, under the hydrogen cycle architecture, the calculation of the hydrogen consumption rate and operating current under different loads is no longer a simple linear relationship. To give a comprehensive optimization of PEMFC operating conditions, it is not only necessary to consider the intrinsic electrochemical characteristics of the cell, but also from the perspective of the entire system. However, current research in this field remains limited, particularly studies adopting a multidisciplinary approach that bridges component-level analysis with system-level dynamics.

1.2.2. System modeling

In actual industrial applications, system simulation has emerged as an indispensable methodology in FCV development. This computational approach enables systematic investigation of energy management strategies [18,19], transient behavior characterization [20], and failure mode diagnostics [21]. A PEMFC system contains a lot of devices that

Fig. 1. Hydrogen application in a zero-carbon city.

provide the fuel or air supply, cooling, power regulation, and system monitoring. It is necessary to integrate them to study the effect of component interaction on the system level. There has been extensive research on these subsystems, most of which are control-oriented [12].

For the anode and cathode gas supply systems, the current research focus is mostly on how to achieve precise control of the flow rate and pressure of the gas reactant [13]. Regarding the thermal management subsystem, to achieve precise control of the stack temperature, scholars have developed many advanced control strategies, including fractional order PID (Proportional-Integral-Derivative) [15], fuzzy PID [16], multi-model predictive [17], cascade internal model control [18]. For the PEMFC stack, current research mostly adopts zero-dimensional models. The output performance of fuel cells is calculated by empirical formulas [22] or an equivalent electrical circuit model [23]. Although it can meet the computational speed requirements of system simulation, the output performance fluctuations caused by operating conditions (such as temperature and humidity) changes under transient conditions cannot be accurately captured. The FCV system's response characteristic, considering the cell performance change caused by operating conditions, has seldom been revealed and analyzed.

The three-dimensional multi-phase model can effectively describe the performance variation under the influence of complex coupled transport processes, but it is difficult to couple into system simulation models. The data-driven surrogate model of performance prediction has developed rapidly nowadays [24] and brings a solution to this problem. Ahmadi et al. [8] trained a deep neural network to predict cell performance degradation. The impacts of the PEMFC degradation phenomenon on the hydrogen fuel cell buses' fuel consumption are evaluated. Yuan et al. [25] utilized the combination of an ensemble learning approach and a wrapping approach to improve the robustness of feature selection and accuracy of PEMFC system performance prediction. However, these machine learning (ML) models have not paid attention to the changes in cell performance caused by operating conditions, nor have they explored the coupling effects of multiple components at the system level.

1.2.3. FCV energy management

To fully harness the advantages of varied energy sources and achieve optimal energy efficiency of FCV, the development of an advanced energy management strategy (EMS) is imperative. Aziz et al. [19] developed and validated a novel coordinated control strategy for a hybrid shipboard power system incorporating multiple PEMFCs and battery energy storage system units. The simulation results showed that the system could reduce the hydrogen consumption by 14.16 % compared with conventional control strategies. Zhang et al. [26] incorporate the air conditioning system into the energy management framework and propose a hierarchical EMS that balances thermal comfort and energy optimization goals. Alhumade et al. [27] proposed a new EMS using the white shark optimizer technique to optimally distribute the load demand between the sources in a hybrid Photovoltaic/PEMFC/Lithium-Ion Batteries/Supercapacitors microgrid.

Frequent load changes can accelerate the PEMFC performance degradation and decrease system stability. Yang et al. [28] conducted experiments using a multi-purpose vehicle equipped with a 45 kW fuel cell system and a 24 kW·h battery. It was found that the larger the variation in the target output power of the PEMFC, the more pronounced the overshoot or undershoot. Li et al. [29] explored how to reformulate the EMS problem within a reinforcement learning framework. Due to the limitations of current computational ability and memory size of the vehicle control unit, integrating this type of EMS onboard and ensuring its stable and reliable operation in physical environments remains challenging. Quan et al. [15] proposed a health-aware model predictive control (MPC) EMS that can effectively reduce the steep drop of the stack hydrogen/oxygen excess ratio, to protect the fuel cell system lifetime. However, the computational complexity of MPC is high, and it's highly dependent on model accuracy. Therefore, there is an urgent need to develop a simple and cost-effective energy management strategy that can achieve efficient energy utilization while reducing fuel cell power fluctuations.

1.3. Contributions and main contents of the present study

The comprehensive optimization of proton exchange membrane fuel cells (PEMFCs) requires consideration of both electrochemical characteristics and system-level dynamics. For fuel cell vehicles, it is urgent to develop efficient and concise energy management strategies to balance energy utilization and fuel cell power fluctuation suppression. In the present study, a multi-level FCV system model is developed, and optimization has been carried out at various scales. The main contributions are as follows:

(1) A comprehensive operating condition optimization is conducted, considering the electrochemical performance of the cell itself and the parasitic power of the system. And the optimal power density/efficiency point was determined.
(2) A system simulation model that incorporates the machine learning performance prediction model is established, which can reflect the performance variation with operating conditions.
(3) A novel fuzzy control-based EMS is proposed, which can not only achieve lower hydrogen consumption, but also smooth the load fluctuation of PEMFC.

The model framework in the present study is illustrated in Fig. 2. Firstly, the machine learning model of performance prediction is trained based on CFD results. The ML model with high accuracy and computational efficiency is adopted as a surrogate objective function. Then, based on the trained ML model, the sensitivity of anode and cathode operating conditions to the output performance of fuel cells was obtained by analysis of variance (ANOVA) method. The selected operation conditions that have a significant impact on the performance are adopted to carry out the optimization with the maximum power density, combined with different intelligent optimization algorithms. After obtaining the optimal operating conditions, the model is introduced into the PEMFC system simulation through the FMU (Functional Mock-up Unit) interface. Considering the anode and cathode gas supply system, the load current at the maximum efficiency of the system is obtained. Finally, the scope is further expanded, and the FCV system simulation model is constructed. Based on the obtained optimal operating conditions and load current, the vehicle power performance and economy under different power distribution strategies are studied.

The article is organized as follows: the model details are elaborated in Section 2. By coupling the machine learning surrogate model, a system simulation model for a fuel cell-lithium battery hybrid power system applied to 4.5-ton refrigerated or logistics vehicles is established. The principle of the proposed fuzzy control-based novel EMS is provided. Then, in Section 3, the optimal operating conditions, load current, dynamic response, and energy analysis obtained from the simulation are displayed and analyzed. Based on the developed powertrain model, the widely recognized New European Driving Cycle (NEDC) is adopted to study the dynamic performance and energy economy of the FCV system under test conditions. Different EMSs are compared in detail, and the superiority of the proposed fuzzy control-based EMS is pointed out. The transient characteristics of temperature, pressure, and flow parameters within the fuel cell system are analyzed. Finally, some conclusions are drawn in Section 4.

2. Methodology

This section will first introduce the system architecture composition of FCVs. Subsequently, the modeling methods for each subsystem were presented, followed by the energy management rules used during system operation. Finally, the numerical methods employed in system

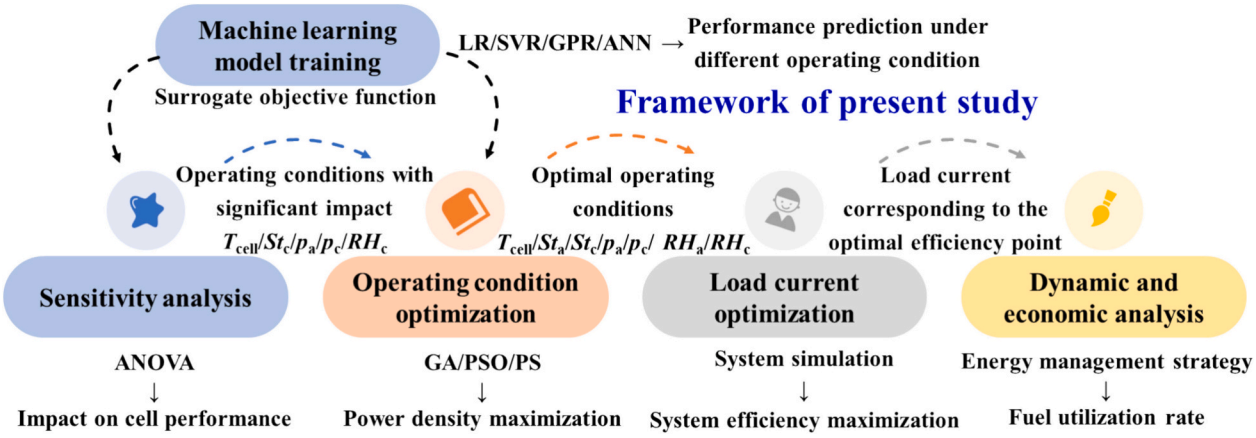

Fig. 2. Workflow of simulation and analysis.

simulation are given.

2.1. System configuration

This study focuses on vehicular fuel cell systems [21,30]. Fig. 3 depicts the powertrain architecture. The 650 V direct current (DC) bus supplies power to the traction motor, with both the fuel cell and lithium battery connected via DC/DC converters. A bidirectional DC/DC converter interfaces with the battery to enable energy recuperation. The red arrows in Fig. 3 indicate energy flow directions.

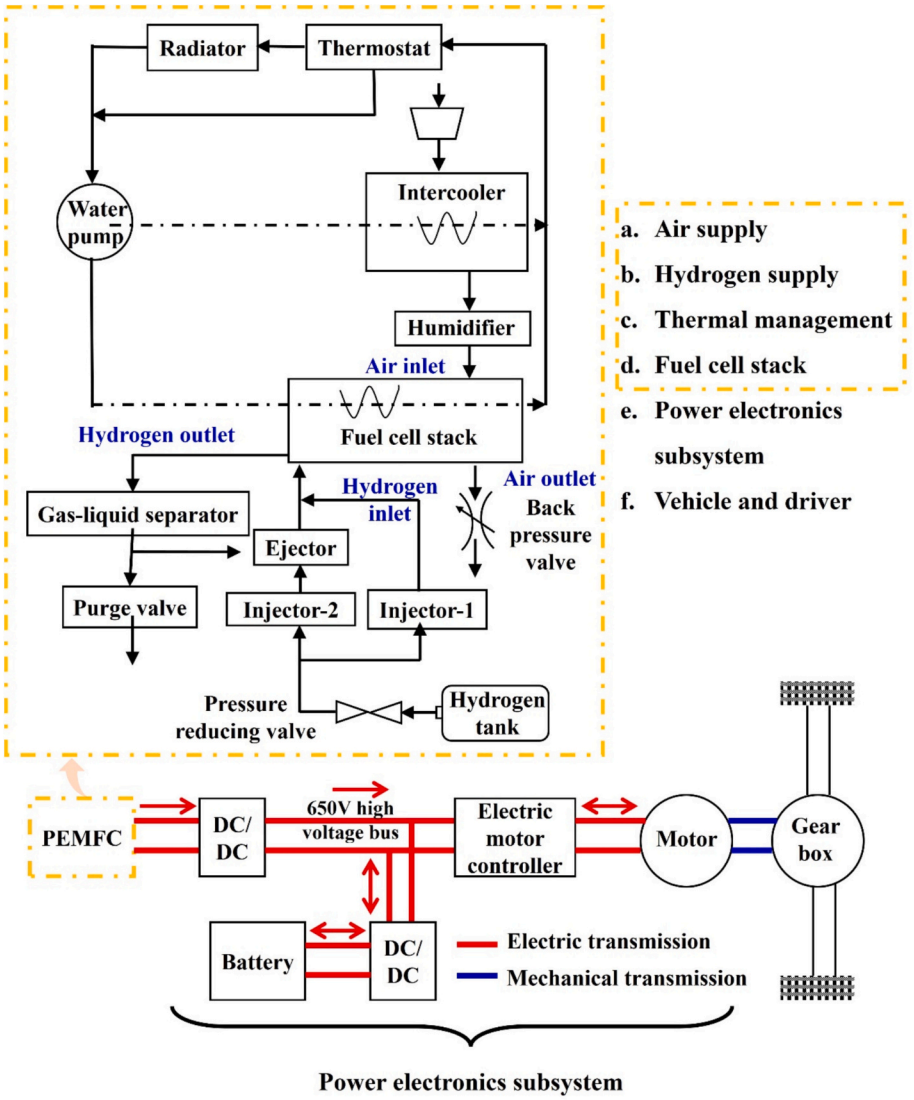

Fig. 3. Schematic of system configuration.

The fuel cell system comprises four subsystems: air supply, hydrogen supply, thermal management, and fuel cell stack. The ambient air undergoes a multi-stage conditioning process before stack entry: initial compression is followed by intercooler-mediated temperature reduction, succeeded by exchanging moisture with the cathode exhaust gas through a membrane humidifier. This precisely conditioned gas reactant subsequently enters the fuel cell stack to participate in the oxygen reduction reaction at the triple-phase boundaries of the cathode catalyst layer. On the anode side, hydrogen stored at 35 MPa is regulated by pressure-reducing valves before entering the stack. A hybrid hydrogen recirculation system combining a fixed-nozzle ejector and dual injectors [31,32] is employed, as shown in Fig. 3. The PID-controlled injectors 1 and 2 adjust anode pressure and flow rates, respectively. Anode exhaust passes through a gas-liquid separator before being purged or recirculated. The thermal management system uses water as a coolant, circulated by a pump to cool both the intercooler and the stack. A thermostat regulates the coolant flow path.

2.2. Sub-model description

2.2.1. Gas and coolant flow

Both gas and coolant flow paths are modeled as interconnected chambers linked by pipelines, and the pressure drop serves as the primary driving force for fluid motion. The state variables (pressure, temperature, species concentration) within spatially distributed chambers can be calculated through the energy/mass conservation and state equations. Considering the difference in physical properties between reactant gas and liquid coolant, particularly regarding compressibility, governing equations for gas and liquid flows are detailed separately.

2.2.1.1. Gas flow. The pressure losses encountered by anode/cathode reactant gases flowing through the cell stack or other components (e.g., anode pressure-reducing valves) are governed by ideal gas isentropic flow assumptions. The resultant mass flow rates q_m (kg·s^{-1}) are calculated via Eq. (1):

$$q_m = \begin{cases} AC_q\sqrt{2\dfrac{\gamma}{\gamma-1}\dfrac{p_0}{v_0}\left[\left(\dfrac{p_2}{p_0}\right)^{\frac{2}{\gamma}}-\left(\dfrac{p_2}{p_0}\right)^{\frac{\gamma+1}{\gamma}}\right]}, \dfrac{p_2}{p_0} > \nu_{cr} \\ AC_q\sqrt{2\dfrac{\gamma}{\gamma+1}\dfrac{p_0}{v_0}\left(\dfrac{2}{\gamma+1}\right)^{\frac{2}{\gamma-1}}}, \dfrac{p_2}{p_0} \le \nu_{cr} \end{cases} \tag{1}$$

where p_0 (Pa) is stagnation pressure, p_2 (Pa) is outlet pressure, v_0 (m^3·kg^{-1}) is stagnation-specific volume, T_0 (K) is stagnation temperature, $\gamma = 1.4$ is the isentropic exponent, p_0(Pa) is outlet pressure, ν_{cr} is critical pressure ratio, A(m^2) is the cross-sectional area of the channel, C_q is discharge coefficient. For the anode ejector, purge valve, and cathode back pressure valve, the flow areas are variable. Therefore, the effective flow area (A) in Eq. (1) dynamically adapts to component actuation states.

When the gas flows through different positions, the state quantity is different. Take the cathode, for example, during gas flow through the intercooler, membrane humidifier, stack inlet manifold, flow channels on the bipolar plate, and stack outlet manifold, the gas mass fraction, pressure, and temperature change accordingly. Their computation needs to combine the conservation equation and the equation of state, which is provided in the Appendix.

2.2.1.2. Liquid flow. The flow rate Q (m^3·s^{-1}) of coolant in a specific pressure difference is calculated as in Eqs. (2)–(4).

$$Q = C_q \times A \times \sqrt{\frac{2|\Delta p|}{\rho}} \times sign(\Delta p) \tag{2}$$

$$C_q = C_{qmax} \times \tanh\left(\frac{2\lambda}{\lambda_{crit}}\right) \tag{3}$$

$$\lambda = \frac{\rho h_d}{\mu} \times \sqrt{\frac{2|\Delta p|}{\rho}} \tag{4}$$

where C_q is the flow coefficient; Δp (Pa) is the pressure drop; h_d (m) is the hydraulic diameter; μ (Pa·s) is the coolant kinetic viscosity; λ_{crit} is an auxiliary coefficient; *sign* is a sign function [33]. In the modeling process, both the frictional and localized resistance of the coolant are characterized by Eq. (2). The temperature and pressure of the coolant in a specific chamber are formulated as follows:

$$\frac{dT}{dt} = \frac{\dot{Q} + \sum dm_i h_i - h\sum dm_i}{\rho c_p V} + \frac{\alpha T}{\rho c_p}\frac{dp}{dt} \tag{5}$$

$$\frac{dp}{dt} = \frac{\beta_T \sum dm_i}{\rho V} + \beta_T \alpha \frac{dT}{dt} \tag{6}$$

where T (K) is the coolant temperature; $\dot{Q}$ (W) is the heat exchanged; $dm_i h_i$ (W) is the enthalpy flow rate at port i; h (J·kg^{-1}) is the enthalpy; p (Pa) is the pressure; ρ (kg·m^{-3}) is the coolant density, c_p (J·kg^{-1}·K^{-1}) is the isobaric specific heat capacity. V (m^3) is the chamber volume. The isothermal bulk modulus β_T (Pa) and the isobaric thermal expansion coefficient α (K^{-1}) are defined in Eq. (7):

$$\begin{cases} \beta_T = \rho \cdot \left(\dfrac{\partial \rho}{\partial p}\right)_T^{-1} \\ \alpha = -\dfrac{1}{\rho} \cdot \left(\dfrac{\partial \rho}{\partial T}\right)_p \end{cases} \tag{7}$$

The key model parameters, such as the chamber volume, the flow area, and the flow coefficient, are listed in Table I.

2.2.2. Air supply subsystem

2.2.2.1. Air compressor. The air compressor is used to deliver clean air with a specific pressure and flow rate for the PEMFC stack. The airflow is determined by finding the operating point in the air compressor MAP diagram. Ignoring the mechanical transmission components, the variation curve of centrifugal air compressor pressure ratio with flow rate and speed $P_r = f(dm_c, w_c)$ is adopted [34], as shown in Fig. 4(a).

Map plots are obtained at reference temperature T_{st} and reference pressure p_{st}. The speed and flow rate before checking the table are corrected according to Eqs. (8) and (9) below:

$$dm_c = dm\sqrt{\frac{T_{up}}{T_{st}}}\frac{p_{st}}{p_{up}} \tag{8}$$

$$w_c = w\sqrt{\frac{T_{st}}{T_{up}}} \tag{9}$$

where T_{up} (K), p_{up} (Pa) are the upstream temperature and pressure, respectively; dm_c (kg·s^{-1}) and w_c (rev·min^{-1}) are the corrected flow rate and speed. Eq. (10) is used to calculate downstream temperature (T_{down}).

$$T_{down} = T_{up} + \frac{T_{up}}{\eta_{is}}\left(Pr^{\frac{\gamma}{\gamma-1}} - 1\right) \tag{10}$$

where T_{down} (K) is the downstream temperature; $\gamma = 1.4$ is the gas adiabatic index; $\eta = 0.8$ is the compressor isentropic efficiency (assumed as a constant). Then the required compressor torque for the rotating shaft can be deduced by Eq. (11)

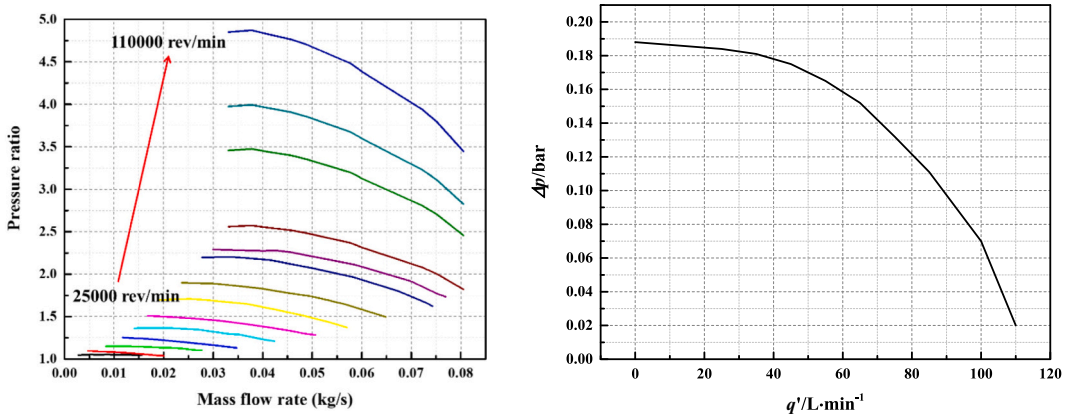

(a) Compressor map (b) Coolant pump map

Fig. 4. Compressor and coolant pump map.

$$\tau = \frac{dmh_{down} - dmh_{up}}{w} \tag{11}$$

where h_{up} (J·kg^{-1}), h_{down} (J·kg^{-1}) are the specific enthalpy of upstream and downstream gases; w (rev·min^{-1}) is the compressor speed.

2.2.2.2. Membrane humidifier. The amount of water diffusion dm_{diff} (kg·s^{-1}) in a membrane humidifier is calculated by Eqs. (12)–(13)

$$dm_{diff} = -D_{diff} A \frac{\rho_{mem}}{M_{mem}} \frac{\lambda_2 - \lambda_1}{\delta_{mem}} M_{H_2O} \tag{12}$$

$$D_{diff} = 4.1 \times 10^{-10} \left(\frac{\lambda_{ave}}{25}\right)^{0.15} \left(1 + \tanh\left(\frac{\lambda_{ave} - 2.5}{1.4}\right)\right) \tag{13}$$

where D_{diff} (m^2·s^{-1}) is the effective diffusion coefficient of membrane water; ρ_{mem} (kg·m^{-3}) and M_{mem} (kg·mol^{-1}) are the density and equivalent mass of the dry proton-exchange membrane (PEM); A (m^2) is the area of the membrane surface in contact with the gas; δ_{mem} (m) is the thickness of the PEM; M (kg·mol^{-1}) is the molar mass of water; λ_1 and λ_2 are the equilibrium membrane water content of the dry and wet sides of the PEM, respectively; λ_{ave} is the average value of λ_1 and λ_2. The λ_1 and λ_2 are related to the local water activity and temperature, as shown in Eqs. (14)–(16)

$$\lambda = \lambda_{eq} = \begin{cases} 0.0043 + 17.81a_w - 39.85a_w^2 + 36a_w^3, 0 < a_w \le 1 \\ 14 + 1.4(a_w - 1), 1 < a_w \le 3 \end{cases} \tag{14}$$

$$a_w = \frac{c_{vapor} RT}{p_{sat}} \tag{15}$$

$$\begin{aligned} \log_{10}\left(\frac{p_{sat}}{101325}\right) = & -2.1749 + 0.02953(T - 273.15) \\ & - 9.1837 \times 10^{-5}(T - 273.15)^2 \\ & + 1.4454 \times 10^{-7}(T - 273.15)^3 \end{aligned} \tag{16}$$

where a_w is water activity; c_{vapor} (mol·m^{-3}) is the vapor concentration; R (J·mol^{-1}·K^{-1}) is the ideal gas constant; p_{sat} (Pa) is saturation pressure.

2.2.3. Hydrogen supply subsystem

2.2.3.1. Hydrogen tank. For gas in a hydrogen tank, the ideal gas equation of state is satisfied as shown in Eq. (17):

$$pV = \frac{m}{M_{H_2}} RT \tag{17}$$

where p (Pa), T (K), m (kg), and V (m^3) are the pressure, temperature, mass, and volume of hydrogen, respectively; M (kg·mol^{-1}) is the molar mass of hydrogen. The related parameters are shown in Table 1.

2.2.3.2. Ejector. To improve the hydrogen utilization rate, the fuel cell system usually recycles the excess hydrogen back to the stack inlet for reuse. In the present study, an ejector is used to recover hydrogen gas from the outlet and humidify the inlet gas. The ejector is mainly composed of three parts: the contraction part, the mixing part, and the diffusion part, as shown in Fig. 5. High-pressure hydrogen gas flows into the ejector from the A port (mass flow rate m_A). It is sprayed out through the nozzle while also suctioning the residual hydrogen gas at port B (mass flow rate m_B). After being mixed in the mixing chamber, the two enter the diffusion tube and are pressurized before entering the fuel cell stack.

The driving flow rate through the nozzle m_A (kg·s^{-1}) can be calculated by Eq. (1), according to the pressure at the A port (p_A) and the ejector outlet pressure ($p_{E,out}$). The equivalent cross-sectional area and discharge coefficient of the nozzle (given in Table 1) are adjusted by trial to achieve a reference entrainment ratio ($ER = m_B/m_A$) of 1.75. Finally, the B-port flow rate m_B (kg·s^{-1}) can be obtained by ER and m_A.

2.2.3.3. Gas-liquid separator. Before entering the ejector, the gas-liquid mixture discharged from the fuel cell stack needs to be separated from the liquid water by a gas-liquid separator. The gas-liquid mixture inlet flow rate m_{in} (kg·s^{-1}) and drainage flow rate for m_{dis} (kg·s^{-1}) satisfy the following equation:

$$m_{in}(1 - Y_{in}) = (m_{in} - m_{dis})(1 - Y_{out}) \tag{18}$$

where Y_{in} and Y_{out} are upstream and downstream water mass fractions. The outlet water mass fraction Y_{out} is set as 80 %. Then the drainage flow rate is

$$m_{dis} = m_{in} \frac{Y_{in} - Y_{out}}{1 - Y_{out}} \tag{19}$$

2.2.4. Thermal management subsystem

2.2.4.1. Intercooler. The temperature rises after air compression, and an intercooler is used to prevent the air inlet temperature from being too high. The high-temperature air transfers heat to the deionized water in the intercooler. The heat transfer capacity of the intercooler is calculated using the efficiency-number of heat transfer units (ε-NTU) method. The heat transfer rate Φ (W) can be calculated as follows:

$$\Phi = (q_m c_p)_{min}(T' - T'')_{max} = \varepsilon (q_m c)_{min}(T_1' - T_2') \tag{20}$$

Table 1
System model parameters.*

Parameters	Value	Unit
Air supply system		
Membrane area*	200	cm^2
Membrane thickness	0.05	mm
Cathode inlet manifold volume	0.4	L
Cathode channel volume	0.3	L
Cathode outlet manifold volume	0.4	L
The cross-sectional area of the stack cathode inlet throttle orifice	0.95/9	cm^2
Flow coefficient of the stack cathode inlet throttle orifice	0.72	
The cross-sectional area of the stack cathode outlet throttle orifice	1.8/9	cm^2
Flow coefficient of the stack cathode outlet throttle orifice	0.72	
Backpressure valve flow coefficient	0.72	
Maximum cross-sectional area of the backpressure valve	8	cm^2
Intercooler heat transfer area	1	m^2
Hydrogen supply system		
The initial mass of the hydrogen cylinder	15	kg
Hydrogen storage pressure	70	MPa
Injector 1/2 flow coefficient	0.72	
Maximum flow area of injector 1/2	0.4/0.55	cm^2
Anode inlet manifold volume	0.4	L
Anode channel volume	0.22	L
Anode outlet manifold volume	0.4	L
The cross-sectional area of the stack anode inlet/outlet throttle orifice	1	cm^2
Flow coefficient of the stack anode inlet/outlet throttle orifice	0.72	
The equivalent cross-sectional area of the nozzle	0.05	cm^2
The flow coefficient of the nozzle	0.72	
PEMFC stack		
Active area	323	cm^2
Cell numbers	330	
Stack mass	30	kg
Thermal capacitance of the stack	710	$J{\cdot}kg^{-1}{\cdot}K^{-1}$
The mass density of the stack	2265	$kg{\cdot}m^{-3}$
Thermal conductivity of the stack	129	$W{\cdot}m^{-1}{\cdot}K^{-1}$
Thermal management system		
The outer diameter of the fan	0.3	m
Radiator length	0.4	m
Radiator height	0.5	m
The coolant chamber volume of the radiator	2	L
Diameter of the coolant pump impeller	18	mm
Reference density for the coolant pump	1049	$kg{\cdot}m^{-3}$
Fluid volume for the coolant pump	0.7	L
Coolant channel volume in the stack	0.3	L
Post-thermostat chamber volume	0.01	L
Equivalent orifice size for large cycles	0.2	m
Maximum flow coefficient for large cycles	0.7	
The auxiliary coefficient for large cycles	1000	
Equivalent orifice size for the stack coolant cycle	0.2	m
Flow coefficient for the stack coolant cycle	0.9	
The auxiliary coefficient for the stack coolant cycle	1000	
Heat transfer area of the stack	2000	cm^2
Convective heat transfer coefficient of the stack	1000	$W{\cdot}m^{-2}{\cdot}K^{-1}$
Traffic		
Vehicle overall mass	4.5	t
Wheel radius	0.34	m
Vehicle rolling resistance factor	0.009	
Wind resistance factor	0.5	
Windward area	2.72	m^2

* It should be noted that the "membrane area" listed in the table is not the PEMFC active area. It is the contact surface area of the membrane humidifier in Eq. (12).

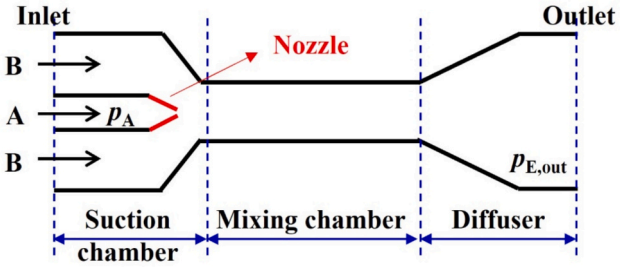

Fig. 5. Hydrogen ejector.

$$\varepsilon = \frac{1 - e^{-NTU\left(1-\frac{(q_m c_p)_{min}}{(q_m c_p)_{max}}\right)}}{1 - \frac{(q_m c_p)_{min}}{(q_m c_p)_{max}} e^{-NTU\left(1-\frac{(q_m c_p)_{min}}{(q_m c_p)_{max}}\right)}} \tag{21}$$

$$NTU = \frac{kA}{(q_m c_p)_{min}} \tag{22}$$

$$\frac{1}{kA} = R_1 + R_2 + R_w \tag{23}$$

where q_m ($kg{\cdot}s^{-1}$) is the mass flow rate; c_p ($J{\cdot}kg^{-1}{\cdot}K^{-1}$) is the specific heat capacity of the fluid; T' (K) and T'' (K) are inlet and outlet temperatures for the cold or hot side, respectively; heat exchanger efficiency ε represents the ratio of actual heat transfer to maximum possible heat transfer; NTU is the number of heat transfer units; k ($W{\cdot}m^{-2}{\cdot}K^{-1}$) is the overall heat transfer coefficient and A (m^2) is the heat transfer area; R_1 ($K{\cdot}W^{-1}$) and R_2 ($K{\cdot}W^{-1}$) are the convective heat transfer thermal resistances on both sides of the heat exchanger wall, and R_w ($K{\cdot}W^{-1}$) is the wall conductive thermal resistance. The heat transfer coefficient k or Nusselt number (Nu) is calculated by the following empirical correlation.

$$Nu = 0.023 Re^{0.8} Pr^{1/3} \tag{24}$$

where Nu, Re, and Pr are the Nusselt, Reynolds, and Prandtl numbers, respectively.

2.2.4.2. Radiator. The radiator is used to cool the high-temperature deionized water. For vehicle fuel cell systems, the calculation of coolant flow on the hot side of the radiator is described in Section 2.2.1.2. The flow rate calculation on the cold side is divided into two parts. In the area affected by the fan, the air velocity needs to be superimposed with the airflow caused by the fan, while in the other part (the remaining windward area), the air velocity is determined by the vehicle speed. Radiator and fan dimensions are shown in Table 1. The heat exchange calculation of the radiator also adopts the ε-NTU method.

2.2.4.3. Coolant pump. The driving force of the coolant comes from the pump. Fig. 4(b) shows the reference curve of the centrifugal water pump, which provides the variation law of the pressure difference of the pump with flow rate q_m ($m^3{\cdot}s^{-1}$) under the reference density ρ ($kg{\cdot}m^{-3}$), reference impeller outer diameter D (mm), and reference speed N ($rev{\cdot}min^{-1}$). Then, by the similarity law of the pump, the pressure difference under a specific flow rate can be calculated as follows.

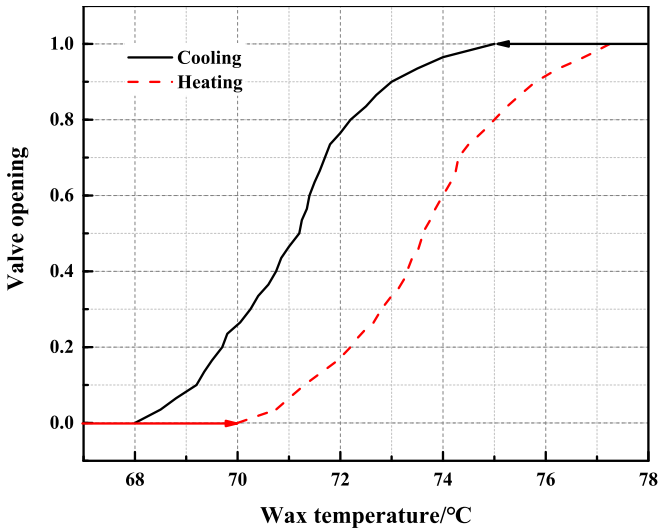

Fig. 6. Thermostat opening curve.

$$q' = \frac{1}{ND^3} q \tag{25}$$

$$\Delta p' = \frac{1}{\rho N^2 D^2} \Delta p \tag{26}$$

2.2.4.4. Thermostat. The role of the thermostat is to control the coolant flow through the radiator and thus regulate the coolant temperature. In the present study, the wax thermostat is adopted, and the curve of the valve opening (to the radiator) as a function of wax temperature is shown in Fig. 6.

The wax temperature T_{wax} (K) is calculated by Eq. (27)

$$\frac{dT_{wax}}{dt} = \frac{1}{\tau}\left(T_f - T_{wax}\right) \tag{27}$$

where T_f (K) is the inlet coolant temperature; τ (s) is the time constant.

2.2.5. Fuel cell stack

In the present study, a data-driven fuel cell stack model is established and adopted. The training datasets are generated by a three-dimensional multi-phase model. Fig. 7 shows that the sub-model includes 8 inputs: anode/cathode pressure, anode/cathode humidity, anode/cathode stoichiometric ratio, temperature, and load current. In the present study, the pairwise testing method [35] is adopted to conduct a design of experiment (DOE) of these 8 variables or factors. According to the factors and corresponding levels shown in Table 2, a total of 139 experiments were designed (as shown in Table S1, see Supplemental Materials). Fig. 8(a) shows the proportion of samples at each level for each factor. Taking temperature as an example, it can be seen that the proportion of 11 levels ranges from 10.1 % to 12.9 %. The sample size at each level is approximately evenly distributed, which proves the rationality of the training dataset design.

In the present study, a steady-state CFD model is used to obtain the training dataset. Nowadays, the fuel cell system has excellent dynamic load performance, which can achieve significant power switching (>30 kW/s) in a short period (~1 s) [5,36]. This means that PEMFC can quickly reach a steady state. In this study, the power fluctuation of the PEMFC stack is less than 30 kW, and the research duration was 1200s. Therefore, it can be considered that the fuel cell stack is approximately in quasi-steady state during this process. The same treatment has been widely adopted in similar research [15,18,27,37,38].

For such a regression prediction problem with 8 inputs and 1 output, four typical machine models, including linear regression (LR), artificial neural network (ANN), support vector regression (SVR), and Gaussian process regression (GPR) are adopted to predict the output voltage under different operating conditions. Introductions of each model can be found in our previous work [39]. The hyperparameters that appeared in different ML models (except for the LR model) are determined by the grid search method. The hyperparameters with the highest accuracy found through 5-fold cross-validation are shown in Table 3. All the data (x_i) are standardized using the Z-score method, as follows:

$$x_i^* = \frac{x_i - \mu}{\sigma} \tag{28}$$

where μ is the average value, and σ is the variance value.

Then, the heat Q (W) generated by the fuel cell stack can be calculated based on the output voltage (predicted by GPR), as follows.

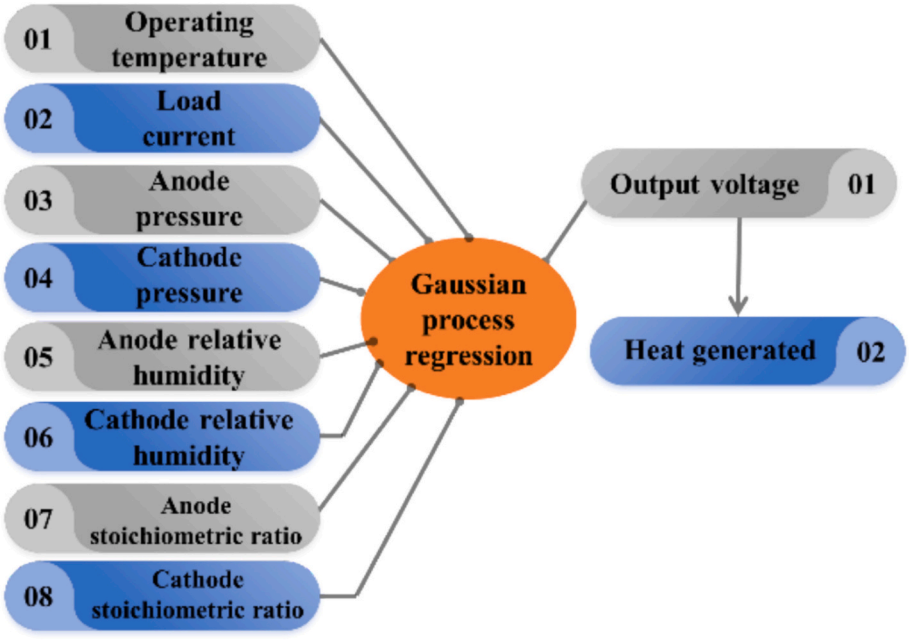

Fig. 7. Prediction of the GPR model [39].

Table 2
Factors and corresponding levels.

Factors	Level
Current density (A·m^{-2})	1000.2000.3000.4000.5000.7000.9000.11000.12000.13000.14000.15000
Temperature (°C)	30,40,50,60,70,78,82,86,90
Anode pressure (bar)	1,2,3,4
Cathode pressure (bar)	1,2,3,4,5
Anode relative humidity	0,10,20,30,40,50,60,70,80,90,100
Cathode relative humidity	0,10,20,30,40,50,60,70,80,90,100
Anode stoichiometric ratio	1.2,1.5,1.7,1.9,3.2,2.4,2.7,3.0
Cathode stoichiometric ratio	1.2,1.5,1.7,1.9,3.2,2.4,2.7,3.0

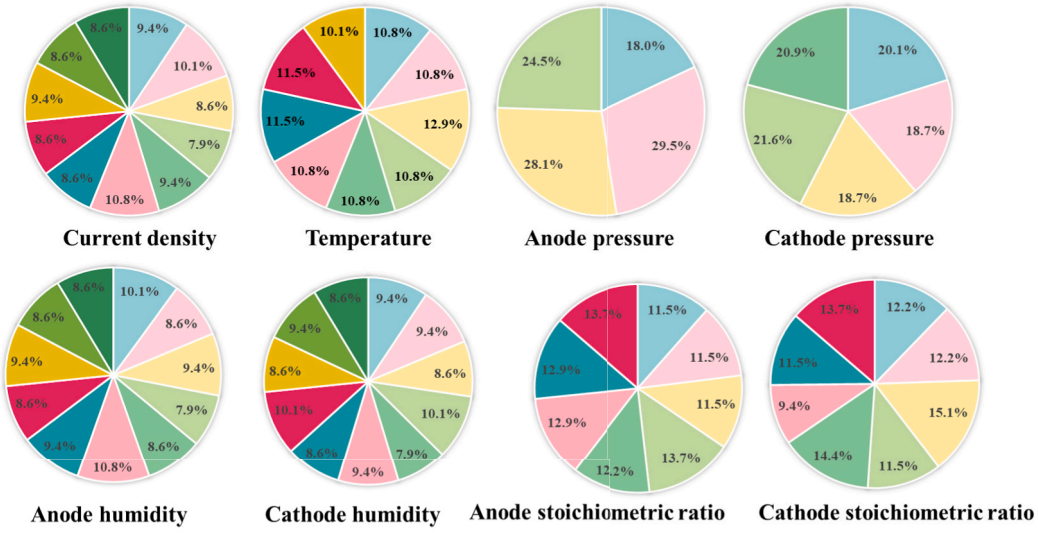

(a) Input variable

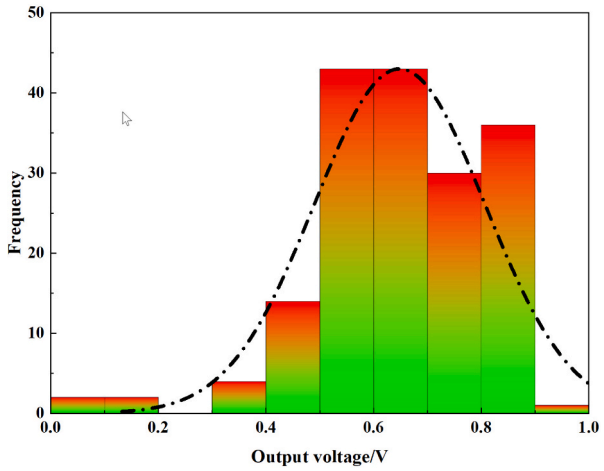

(b) Output voltage

Fig. 8. Sample distribution in the training dataset.

$$Q = N(E_{rev} - V_{out})I \tag{29}$$

$$E_{rev} = 1.229 - 0.846 \times 10^{-3}(T - 298.15) + \frac{RT}{2F}\left(ln\frac{p_{in,H_2}}{p_0} + \frac{1}{2}ln\frac{p_{in,O_2}}{p_0}\right) \tag{30}$$

where N is the number of cells; E_{rev} (V) is the reversible voltage; I (A) is the load current; p_{in,H_2} (Pa) and p_{in,O_2} (Pa) are the partial pressure of inlet hydrogen and oxygen, respectively.

2.2.6. Power electronics subsystem

2.2.6.1. Motor. The electrical energy input to the motor is converted into mechanical energy and thermal energy. Therefore, the following equation of the motor is satisfied:

$$U{\cdot}I = Torque{\cdot}w + dh \tag{31}$$

where U (V), I (A) are the voltage and current input to the motor; *Torque*

Table 3
Hyperparameters of ML models.

ML model	Hyper-parameters
SVM	Box constraint = 10; Kernel scale = 10; Epison = 0.027887
GPR	Covariance function: non-isotropic Matern 3/2; Sigma = 0.021599; Kernel scale = 1000
ANN	Sizes of fully connected layerss = [300 24 84]; Activation functions: Sigmoids; Regularization term strength (Lambda) =7.3803e^{-7};

(N·m), w (rad·s^{-1}) are the motor torque and speed, respectively; dh (W) is the motor heat loss power. The torque is related to vehicle dynamics, and the speed is determined by the vehicle speed. These details are described in Section 2.2.7.

2.2.6.2. Battery. In this study, a lithium-ion (Li-ion) battery is used as an auxiliary power source. The state of charge (SOC) is calculated from equation Eq. (32)

$$\frac{dSOC}{dt} = \frac{I}{C} \times 100\% \tag{32}$$

where I (A) is the battery current and C (Ah) (fixed as 100 Ah) is the battery capacity.

2.2.6.3. DC/DC converter. Before supplying to the motor, the PEMFC output voltage needs to be converted to a high level. The energy transfer through DC/DC is calculated based on Eq. (33):

$$\eta = \frac{U_{out} \cdot I_{out}}{U_{in} \cdot I_{in}} \tag{33}$$

where U_{in} (V), I_{in} (A) are the input voltage and current; U_{out} (V), I_{out} (A) are the converted output voltage and current. In this study, the conversion efficiency η is set as 0.95.

2.2.7. Vehicle and driver

2.2.7.1. Vehicle dynamics. As shown in Fig. 9, the forces received during running are mainly classified into two types: traction and resistance.

The total resistance of the vehicle consists of slope resistance F_i (N), rolling resistance F_f (N), and air resistance F_w (N), see Eq. (34).

$$\begin{cases} F_i = Mg\sin\alpha \\ F_f = Mg\cos\alpha f \\ F_w = 0.5 \times \rho C_d A v^2 \end{cases} \tag{34}$$

where M (kg) is the mass of the vehicle; α is the slope angle; f is the vehicle roll resistance coefficient; C_d is the wind resistance coefficient; A (m^2) is the windward area; v (m·s^{-1}) is the vehicle speed. The acceleration a (m·s^{-2}) of the vehicle is calculated by Eq. (35)

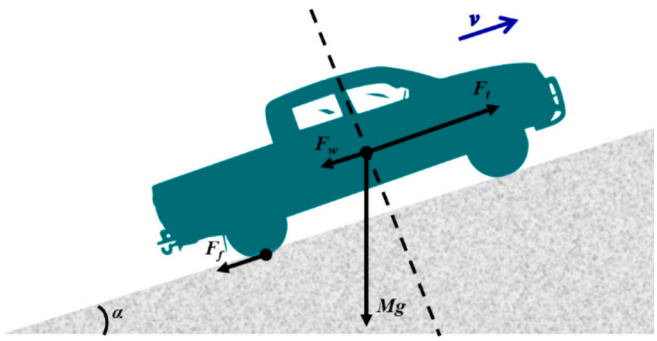

Fig. 9. Vehicle forces.

$$a = \frac{F_t - F_i - F_f - F_w}{M} = \frac{\frac{T_M - T_b}{R} - F_i - F_f - F_w}{M} \tag{35}$$

where F_t (N) is the traction force; T_M (N·m) and T_b (N·m) are the driving and braking torque on the wheels; R (m) is the radius of the wheels.

2.2.7.2. NEDC driving cycle. In this study, the widely recognized NEDC (New European Driving Cycle) cycle is used, which consists of a combination of four typical Urban Driving Cycles (UDC) and one typical Suburban Driving Cycle (Extra Urban Driving Cycles (EUDC)), as shown in Fig. 10. The time, distance, maximum speed, average speed, idling time for UDC, EUDC, and NEDC are given in Table 4.

2.2.8. Energy management strategy

Three energy management strategies (EMSs), constant power output (Scheme A), power following (scheme B), and fuzzy control-based (scheme C) are set up. The details are described as follows.

In scheme A, the fuel cell output power is fixed as P_{oe} (kW), where the PEMFC system achieves the optimum efficiency (see Section 3.5). When the motor demand power (P_m) is less than P_{oe}, the additional electric power output from the fuel cell is partly to drive the motor, and partly to recharge the battery; when is greater than P_{oe}, the battery and the fuel cell jointly provide energy. When the vehicle brakes (the motor works as a generator), the fuel cell and generator jointly charge the Li-ion battery.

In scheme B [8], the PEMFC power varies between the minimum value of 10 kW and the maximum value of 50 kW, as shown in Fig. 11. When P_m is less than 10 kW, excess electricity from the fuel cell can be charged into the battery. When P_m is 50 kW or more, the fuel cell output power is taken as its upper limit of 50 kW. When P_m is located in the range of 10–50 kW, there are two situations. If the battery needs to be recharged and P_m is less than P_{oe}, the fuel cell output is constant at P_{oe}. Otherwise, the fuel cell power varies with P_m.

In this study, in addition to the conventional constant power (scheme A) and power following (scheme B) EMS, a fuzzy control-based (scheme C) EMS is proposed. It consists of two parts, fuzzy control and sliding average filtering, as follows.

Firstly, about fuzzy control, as in scheme B, the motor demand power (P_m) and battery real-time SOC are input into the fuzzy-based controller to obtain the fuel cell output power P_{fc} (unfiltered). The membership function range of P_m (kW), SOC, and P_{fc} (kW) are (−100, 80), (0,1), and (10, 50), respectively. These three variables are all divided into five fuzzy sets, corresponding to values from small to large (ES, S, M, L, EL). The membership function curve is shown in Fig. 12. According to the actual operating conditions, the range where the P_m is negative, corresponding to the power generation state, is divided into the extremely small (ES) set. The range where the SOC is less than 60 % is divided into the ES set. In contrast, the set partitioning of P_{fc} is relatively uniform.

The results of fuzzy control are closely related to the formulation of fuzzy rules. When the motor is used as a generator (corresponding to the ES state of P_m), the output power of the fuel cell should be as small as possible. As the P_m increases, the P_{fc} also gradually increases. Under the same P_m, when the SOC is high, the corresponding P_{fc} is low. According to the above principles, the formulated fuzzy control rule is shown in Table 5. After P_m and SOC are input into the controller, P_{fc} (unfiltered) can be obtained through fuzzification, fuzzy inference, and defuzzification processes.

Then, the output of the controller will be processed by the sliding average filtering algorithm (SAFA). It can make the output power of fuel cells smoother, avoid the generation of high-frequency output power, and increase the lifespan of fuel cells. The SAFA smooths the signal by calculating the mean of data within a fixed window, as shown in Eq. (36).

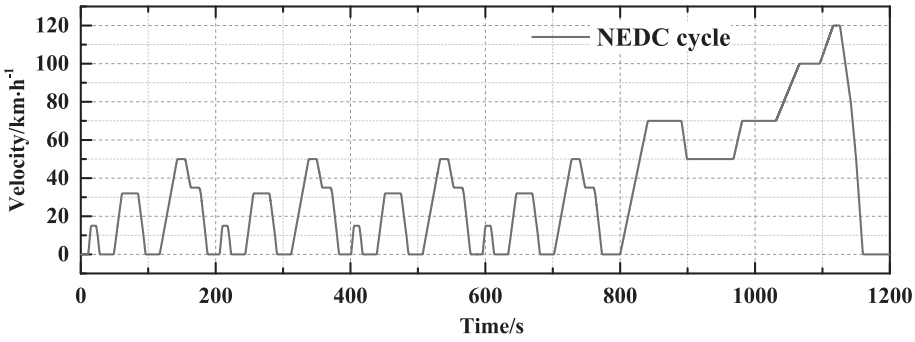

Fig. 10. NEDC cycle.

Table 4
Working condition parameters.

	UDC	EUDC	NEDC
Time/s	195	400	1184
Distance/km	0.99	6.95	10.93
Maximum speed/km·h^{-1}	50	120	120
Average speed/km·h^{-1}	18.26	62.44	33.21
Idle time/s	64	42	298

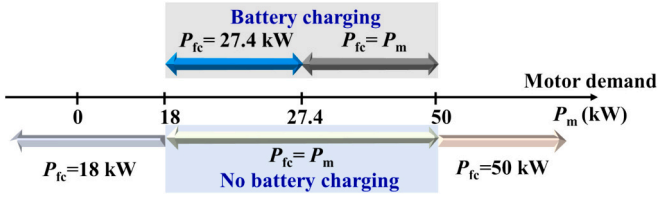

Fig. 11. Energy management strategy of scheme B.

$$P_{fc} = \frac{1}{N}\sum_{t=0}^{N-1} P_T(T-t) \tag{36}$$

where $N = 3$ is the number of data points in the sliding window; t is the sampling time; P_T is the output power of the fuel cell at time T (unfiltered). And zero padding strategy is adopted at the boundary.

2.3. Numerical procedure

In this study, both the training of machine learning models and optimization algorithms are carried out on MATLAB 2024b. All the models except the stack were built in Simcenter Amesim. Simcenter Amesim employs the power bond graph [40] theory for multidomain system modeling. Components are interconnected through predefined topological relationships. Then the Simcenter Amesim standard integrator performs integration in a series of discrete steps. For evaluating the influence of operating conditions on stack and system performance during dynamic operation, the Matlab/Simulink interface added in Amesim is used to realize data exchange. The real-time operating parameters of Amesim, such as load current, temperature, pressure, and stoichiometric ratio, are processed in MATLAB/Simulink to calculate PEMFC voltage and generated heat. In addition, the fuzzy controller proposed in this study is also implemented in MATLAB/Simulink. Real-time data exchange between MATLAB and AMESIM is achieved through the FMU interface.

3. Results and discussion

3.1. Comparison of PEMFC ML models

Fig. 13 shows the ML model-predicted and physical model-simulated output voltage. The test dataset contains a total of 20 samples, shown in Table S1. The training set and test set data in the figure are represented by symbols of different colors and shapes. For LR (Fig. 13(a)) and SVR (Fig. 13(c)), the prediction deviation is large when the output voltage is lower than 0.4 V. This could be explained by the output voltage histogram, as shown in Fig. 8(b). The training samples with output voltage lower than 0.4 V are scarce, which leads to the poor regression effect of the model in this interval. To quantitatively and intuitively compare the performance of various ML models, three error metrics—root mean squared error (*RMSE*), squared correlation coefficient (R^6), and mean absolute error (*MAE*) are introduced to evaluate model performance, as follows.

$$RMSE = \sqrt{\frac{1}{N}\sum_{i=1}^{N}(Y_i - y_i)^2} \tag{37}$$

$$R^2 = 1 - \frac{\sum_{i=1}^{N}(Y_i - y_i)^2}{\sum_{i=1}^{N}(y_i - \bar{y}_i)^2} \tag{38}$$

$$MAE = \frac{1}{N}\sum_{i=1}^{N}|Y_i - y_i| \times 100 \tag{39}$$

The performance indicators of each model are calculated and listed in Table 6. From Fig. 13 and Table 6, it can be observed that on the training set, the GPR model is optimal for all three metrics, followed by ANN, SVM, and LR. Obviously, the LR model struggles to capture the nonlinear relationship between PEMFC performance and operating conditions, although the time consumption of the LR model is extremely short. On the test set, the above conclusion still holds true for *RSME* and R^2 metrics. As for *MAE*, the differences between different models are relatively small, ranging from 0.071 to 0.096. Except linear model, the training time of the other three models is similar. The GPR model has the fastest prediction speed and a relatively moderate model size, which is suitable for deployment applications. Therefore, in the subsequent system modeling, the GPR model will be used to predict the performance of PEMFC.

3.2. Model validation

A comprehensive validation has been carried out to validate the system model. The relevant operating parameters for comparison are the same as the experimental conditions; please refer to the relative literature [5,41,42] for details.

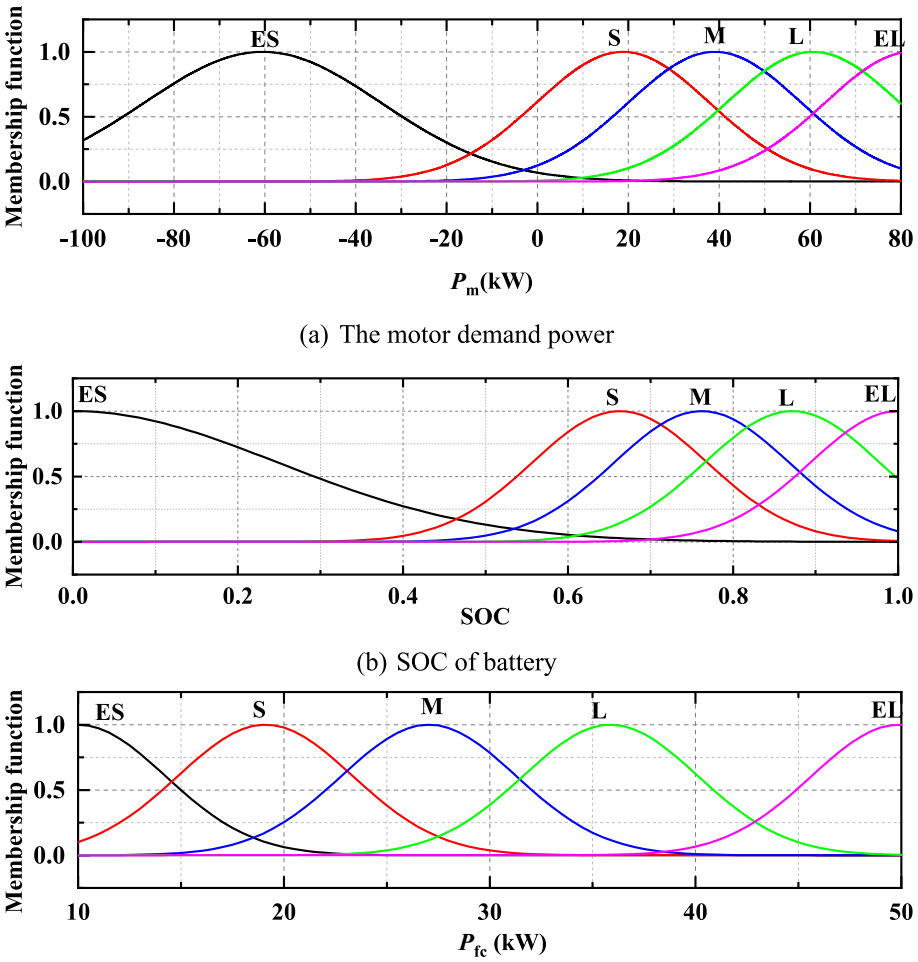

Fig. 12. Membership function of fuzzy control.

Table 5
The fuzzy control rules of P_{fc}.

SOC	P_m				
	ES	S	M	L	EL
ES	S	M	L	EL	EL
S	ES	S	L	EL	EL
M	ES	S	L	EL	EL
L	ES	S	M	L	EL
EL	ES	S	S	M	L

For the air supply and hydrogen recirculation sub-system, their most important role is to appropriate flow rate and pressure for PEMFC. Therefore, the pressure drop under different current densities (corresponding to different gas mixture flow rates) is compared with the experimental data [41]. (see Fig. 14(a)) The maximum deviation of the pressure drop is about 8 %. For the PEMFC performance prediction model, three polarization curves under different inlet pressures and stoichiometric ratios are used for calibration, which ensures the ML model's robustness across multi-scenario applications. (see Fig. 14(b)) The maximum relative error is less than 5 %.

For transient situations, the PEMFC's electrical and thermal performance is validated under transient load conditions [5,42] to verify its adaptability to dynamic environments. In Fig. 14(c), a step current density load from 0.5 A·cm^{-2} to 0.9 A·cm^{-2} and then to 0.6 A·cm^{-2} is applied, and the maximum absolute and relative error of the output voltage are less than 0.02 V and 1.0 %. In Fig. 14(d), the stack temperature is monitored during power switching. It shows that the simulation temperature variation agrees well with the experimental value, especially the time interval when the temperature reaches stability is consistent with the experiment.

3.3. Sensitivity analysis of the operating condition of the PEMFC stack

Analysis of variance (ANOVA) is a statistical method that is used to check the impact of one or more factors by comparing the means of different groups [43]. The experimental data in the ANOVA are obtained by the GPR model, and the operating conditions are set at low, medium, and high levels according to the actual operating condition range. Table 7 shows the designed three-level full factorial design plan, with a total of $3^8 = 6561$ test points. Table 8 presents the ANOVA results.

The critical *p*-value used for statistical significance for this ANOVA was 0.05. If the *p*-value corresponding to the factor's *F* statistic is less than 0.05, that is, under this condition, the factor's influence on the output voltage is particularly significant. It can be seen from the results listed in Table 8 that current density, temperature, anode pressure, cathode pressure, cathode humidity, and cathode stoichiometric ratio have particularly significant effects on output voltage. The influence of anode humidity and anode stoichiometric ratio is not significant; that is, the cell performance is not sensitive to anode humidity and stoichiometric ratio. Similar conclusions are also pointed out by Zhou et al. [14], that the influence of anode operating conditions is much smaller than that of the cathode.

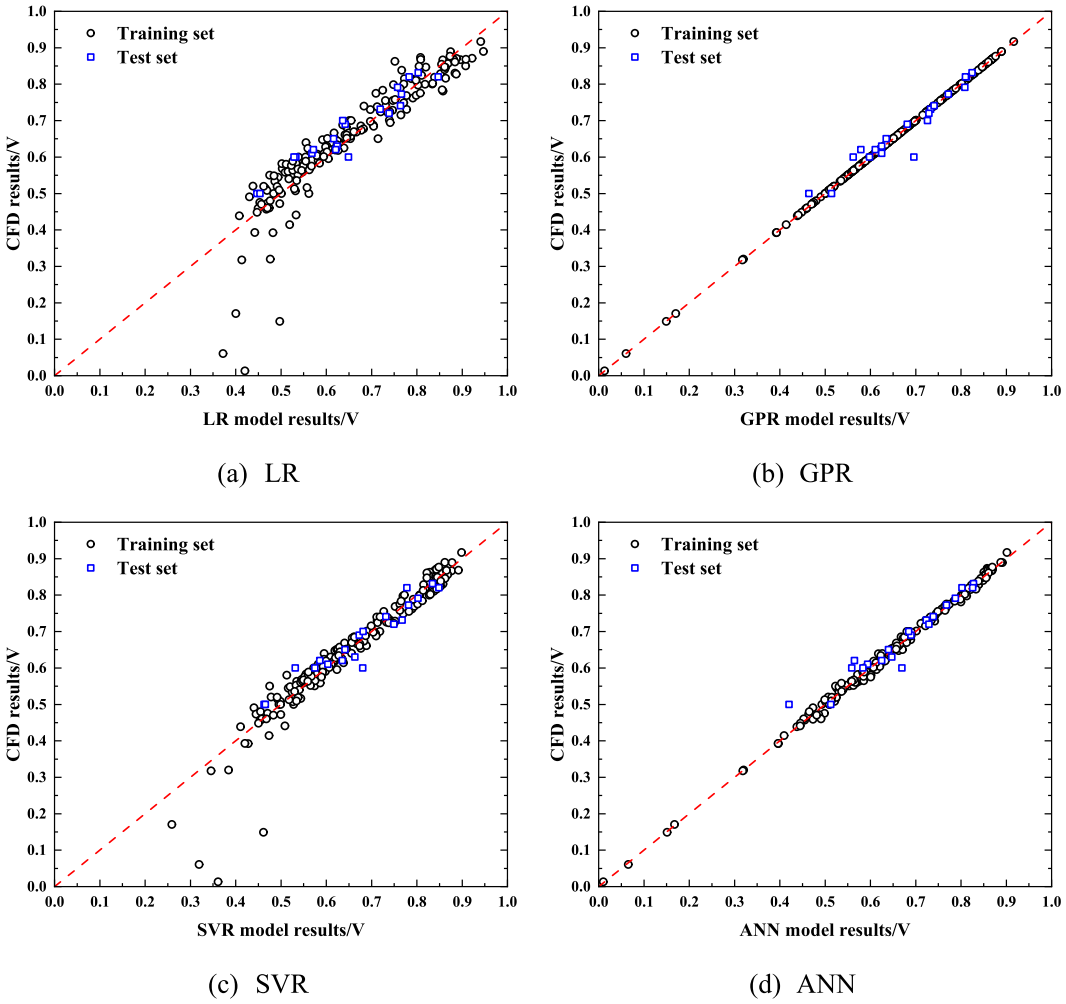

Fig. 13. Prediction of ML models.

Table 6
Comparison of regression effects of ML models.

		Linear	SVM	GPR	ANN
RSEM	Training set	0.0647	0.0469	0.0001	0.0096
	Test set	0.0410	0.0337	0.0281	0.0298
R^2	Training set	0.8326	0.9121	1.0000	0.9963
	Test set	0.8242	0.8810	0.9173	0.9069
MAE	Training set	0.4079	0.3483	0.0006	0.0310
	Test set	0.0710	0.0808	0.0963	0.0793
Training time (s)		1.114079	303.3979	307.1222	321.535
Model size (bytes)		10,944	8685	21,732	104,426
Prediction speed (obs/s)		15,329.9	12,637.66	9580.222	11,269.82

3.4. Operating condition optimization

As mentioned above, the cell performance is not sensitive to anode humidity and stoichiometric ratio. Besides, the performance of PEMFC increases monotonously with the increase of the anode and cathode pressure. Therefore, considering the actual engineering value, the anode pressure ($p_a = 2$ bar), the cathode pressure ($p_c = 1.5$ bar), the anode relative humidity ($RH_a = 100$ %), and the anode stoichiometric ratio ($St_a = 1.5$) are fixed. The remaining operating conditions, including the current density (I), temperature (T), cathode humidity (RH_c), and cathode stoichiometric ratio (St_c) are optimized. Through the GPR cell performance prediction model described in Section 2.2.5, the output voltage can be predicted. The power density is regarded as the objective function. The mathematical expression of the optimization problem is as follows:

$$\max P = UI = f(I, T, p_a, p_c, RH_a, RH_c, St_a, St_c)^* I \tag{40}$$

$$\text{subject to} \begin{cases} 0 < I \le 25000\text{A/m}^2 \\ 60^\circ\text{C} < T \le 90^\circ\text{C} \\ 1 < St_c \le 4 \\ 0 < RH_c \le 100\% \\ p_a = 2\text{ bar}, p_c = 1.5\text{ bar}, St_a = 1.5, RH_a = 100\% \end{cases} \tag{41}$$

The gradient information can not be obtained by the GPR model. This study used three stochastic optimization algorithms, namely genetic algorithm (GA), particle swarm optimization (PSO), and pattern search (PS), to carry out the optmization. Among them, GA and PSO are based on biological evolution and bird swarm search, respectively, while PA directly searches for neighboring points according to certain rules. The relevant parameter settings for the three algorithms are shown in Table 9.

Fig. 15(a) shows the optimization process curves of the different algorithms. With the increase of the iteration number, the power density gradually stabilized to its maximum value. It can be observed that the GA has the fewest number of objective function calls during the calculation process, that is, it quickly finds the optimal operating conditions and determines the peak power density. Moreover, the peak power density obtained by PS optimization is lower than that obtained by GA and PSO. For GA and PSO, the fuel cell in this study reached a peak power density of 9606.80 W·m^{-2} at 19549.99 A·m^{-2}, 61.86 °C (T_{stack}), 100 % cathode relative humidity (RH_c), and a cathode stoichiometric

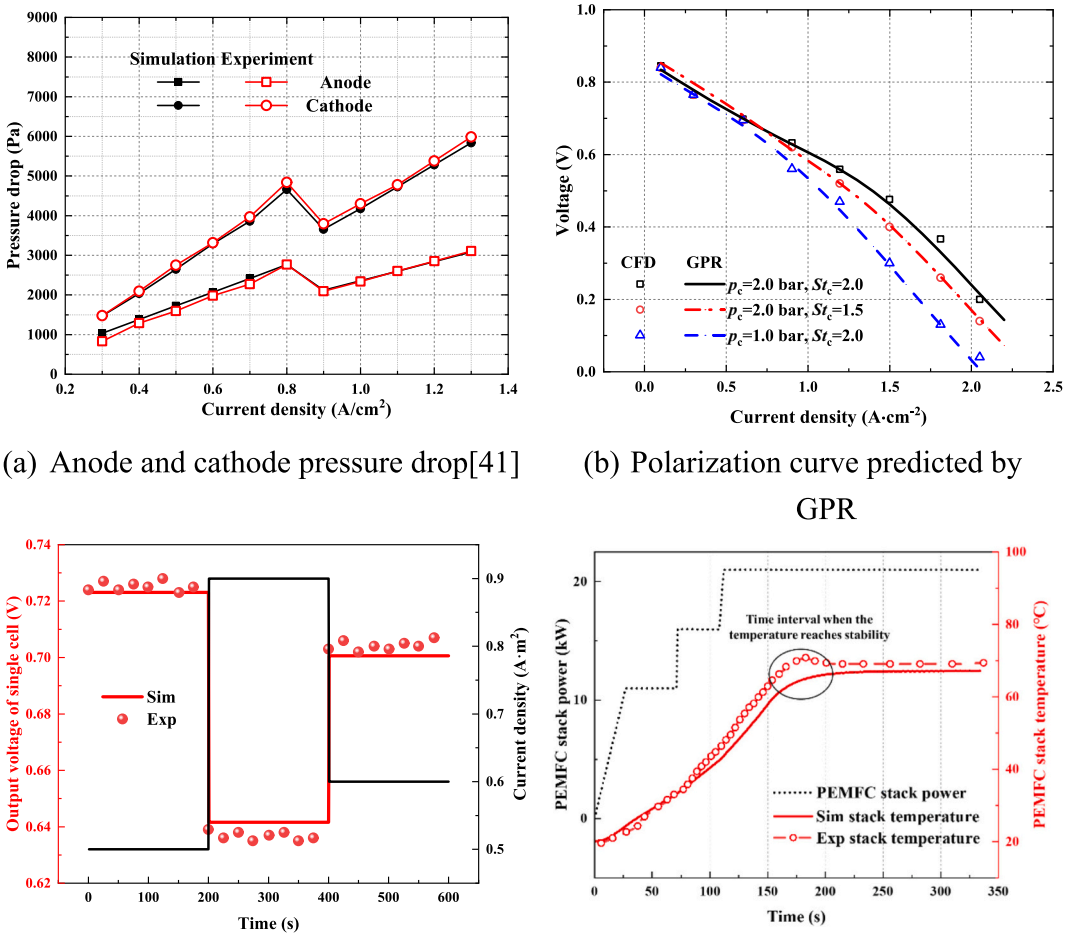

(a) Anode and cathode pressure drop[41]

(b) Polarization curve predicted by GPR

(c) Transient electrical performance[5]

(d) Transient thermal performance[42]

Fig. 14. Model validation.

Table 7
Full factorial design plan.

Factor	Low	Medium	High
Current density	5000	10,000	15,000
Temperature	40	65	90
Anode pressure	1	2	4
Cathode pressure	1	2	4
Anode relative humidity	30 %	60 %	90 %
Cathode relative humidity	30 %	60 %	90 %
Cathode stoichiometric ratio	1	2	3
Anode stoichiometric ratio	1	2	3

ratio (St_c) of 3.4. To demonstrate the superiority of the optimization results, three operating conditions including stack temperature (65, 70, and 75 °C), cathode relative humidity (30, 70, and 100 %), and cathode stoichiometric ratio (1, 2, and 3) are set at low, medium, and high levels according to the actual operating condition range. As shown in Table S1 (see Supplemental Materials), there are a total of 27 cases (full factorial design). The peak power density corresponding to each case is obtained through prediction, as shown in Fig. 15(b). The maximum power density among them is 9552.4 W·m^{-2}, which is lower than the optimized result. For comparison, the polarization curve corresponding to the reference working condition (the stack temperature 70 °C, the cathode relative humidity 100 %, and the cathode stoichiometric ratio 2.0) is also given in Fig. 15(c), and its peak power density is only 8691.5 W·m^{-2}. Compared with the reference condition, the operating point determined by the GA or PSO can increase the peak power density by 10.5 %.

Table 8
Analysis of variance.

Source of variation	Sum of squares	Degrees of freedom	Mean square	*F*-value	*p*-value
Model	181.03	16	11.31	1521.82	$<10^{-4}$
Current density	120.32	2	60.16	8091.53	$<10^{-4}$
Temperature	2.72	2	1.36	183.21	$<10^{-4}$
Anode pressure	0.7038	2	0.3519	47.33	$<10^{-4}$
Cathode pressure	36.75	2	18.38	2471.8	$<10^{-4}$
Anode humidity	0.0024	2	0.0012	0.1626	0.85
Cathode humidity	0.1043	2	0.0521	7.01	0.0009
Anode stoichiometric ratio	1.91×10^{-10}	2	9.541×10^{-11}	1.283×10^{-8}	1
Cathode stoichiometric ratio	20.42	2	10.21	1373.49	$<10^{-4}$
Residual	48.65	6544	0.0074		
Total	229.68	6560			

3.5. PEMFC load point of optimum efficiency

Sections 3.3 and 3.4 were carried out using the cell stack performance prediction model (described in Section 2.2.5), without considering the auxiliary equipment. In addition to the gas supply parameters, the optimal load current of PEMFC also needs to be determined. Considering the main parasitic power from the air compressor and coolant pump in the PEMFC system. The system efficiency η is calculated by Eq. (42)

Table 9
Key parameters of three optimization algorithms.

Algorithom	Key parameters	Value
GA	Population size	50
	Crossover fraction	0.6
	Max stall generations	100
	Selection function	Roulette wheel selection
PSO	Swarm size	200
	Min neighbors fraction	0.75
PA	Max Iterations	1,000,000
	Max function evaluations	1,000,000

$$\eta = \frac{UI - P_{\text{compressor}} - P_{\text{pump}}}{\dot{n}_{H_2} \cdot \Delta h_{\text{rxn}}} \tag{42}$$

where U (V), I (A) are the output voltage and current of the PEMFC stack; $P_{\text{compressor}}$ (W), P_{pump} (W) are the power consumption of the air compressor and coolant pump, respectively. $\dot{n}_{H_2}$ (kg·s^{-1}) is the hydrogen consumption rate; Δh_{rxn} (241 kJ·mol^{-1}) is the low heat value of hydrogen [44]. Both the air compressor ($P_{\text{compressor}}$) and coolant pump (P_{pump}) are rotating machinery, and their power consumption P can be calculated according to Eq. (43)

$$P = \frac{Torque \cdot w}{\eta_p} \tag{43}$$

where *Torque* (N·m), w (rad·s^{-1}), and η_p are the torque, speed, and efficiency of the corresponding rotating machinery, respectively.

When the power of the fuel cell changes, that is, the current changes, the hydrogen consumption ($\dot{n}_{H_2}$) and parasitic power ($P_{\text{compressor}}$ and P_{pump}) will also change accordingly. There exists a suitable current value that allows the system efficiency η to be maximized. In the present study, the variation of system efficiency with the change of PEMFC load current is studied. At each current level, the optimal operating conditions (RH_a = 100 %, RH_c = 100 %, St_c = 3.4, and T_{stack} = 62 °C) obtained in Section 3.4 are adopted, and other operating conditions are selected according to practical experience. The pressure and stoichiometric ratio of the anode and cathode are shown in Fig. 16 and explained as follows.

As shown in Fig. 16(a), with the increase in flow rate, the pressure level of the anode and cathode rises synchronously. The anode pressure is always higher than the cathode pressure, which prevents the air on the cathode side from penetrating the anode under the pressure difference. When air meets hydrogen on the anode side, hydrogen peroxide is easily formed at low potentials, which can cause attenuation of the proton exchange membrane. At the same time, considering the structural strength of the proton exchange membrane, this pressure difference can not be too large, and finally, a pressure difference of about 50 kPa is selected. Fig. 16(b) shows the change of cathode and anode stoichiometric ratio with load current. In a small current density region, to maintain the high pressure of the anode side while improving the cell performance, the anode stoichiometric ratio St_a is high. As the current increases, it gradually decreases from 3 to 1.5. After the current is greater than 80 A, it is maintained at around 1.5.

As shown in Fig. 17(a), the cell stack power, compressor power, and coolant pump power all increase with the load current. The fuel cell stack has not yet reached its peak power, and its power increases with the increase of load. The power of the compressor also increases with the

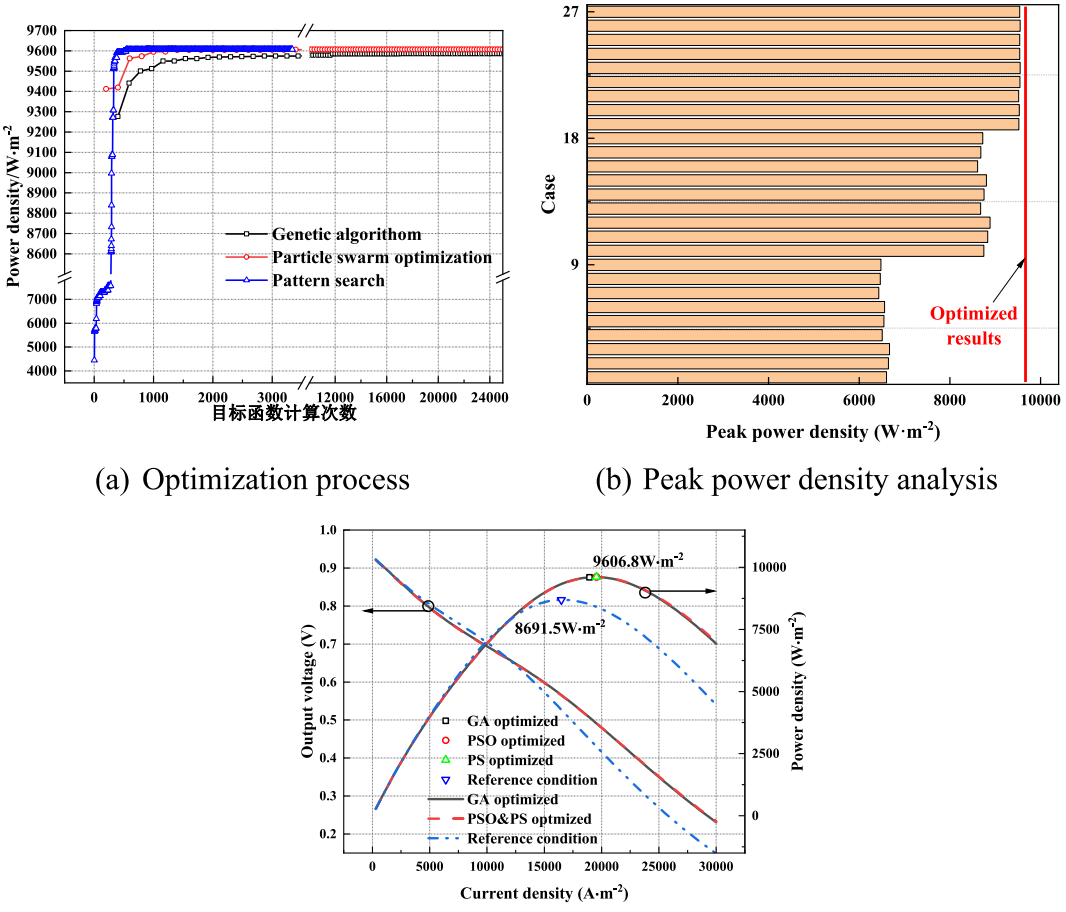

Fig. 15. Operating condition optimization.

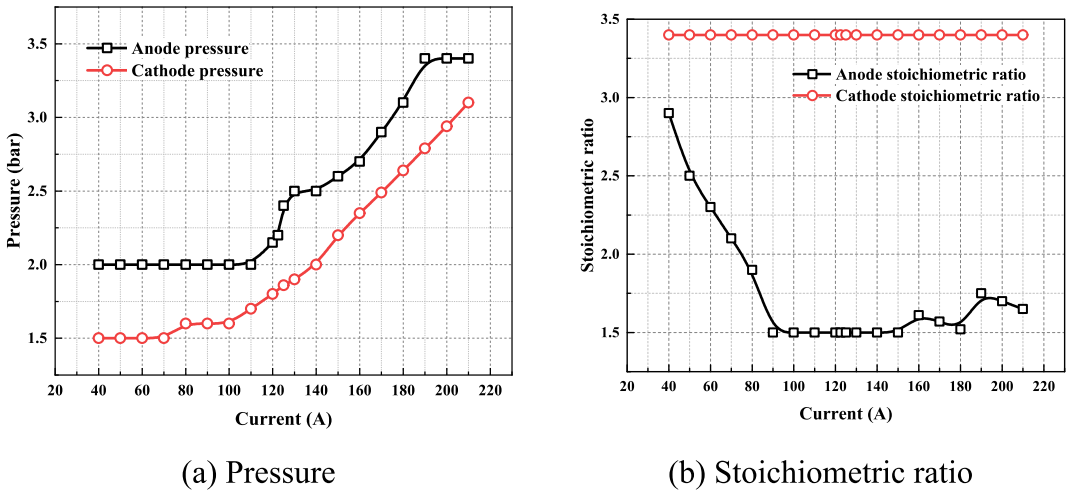

Fig. 16. Operating conditions at different load currents.

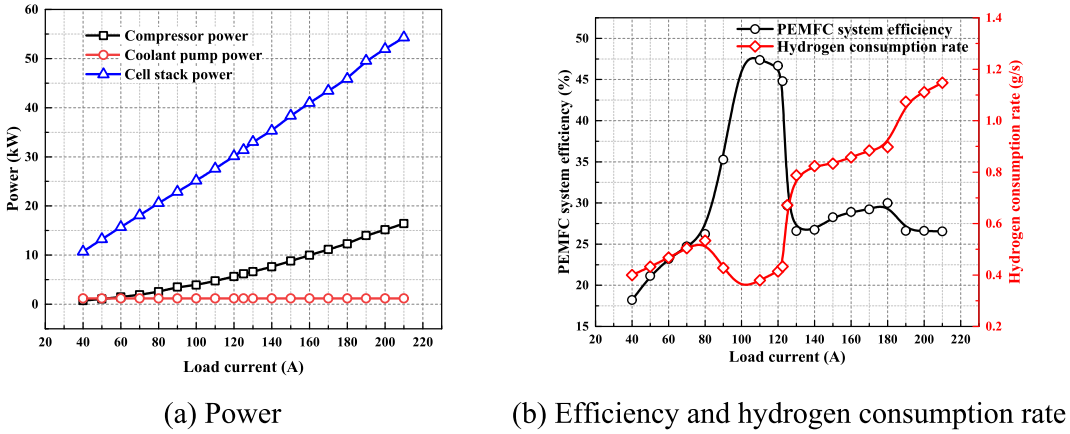

Fig. 17. Analysis of power and efficiency.

increase in the current, which is due to the increase in cathode air flow rate and pressure. Although the power consumption of the coolant pump slightly increases with the current, its power consumption is less than 1 kW in the range of 40–210 A. Therefore, the air compressor is the main parasitic power of the fuel cell system.

Fig. 17(b) shows the calculated efficiency and hydrogen consumption rate curves of the fuel cell system. According to Eq. (42), the system efficiency is negatively correlated with the hydrogen consumption rate. In the range of 90–120 A, the hydrogen consumption rate is significantly lower, even lower than the hydrogen consumption rate of 23–25 g/s at 60–80 A. Within this range, the system efficiency also peaks. At a current of 110 A or a stack power of 27.4 kW, the system efficiency reaches a peak of 47.4 %. This is due to the architecture of the hydrogen circulation system in the present study. The explanation for the change in hydrogen consumption rate is as follows.

At a low current of 40–80 A, injector 1 opens, and injector 2 closes, as shown in Fig. 18(a). The opening of injector 1 is controlled by PID to maintain a pressure of 2.0 bar on the anode side. As mentioned earlier, the anode stoichiometric ratio (St_a) is very high at a low current, reaching 3 at 40 A. At this point, injector 2 is closed under the feedback

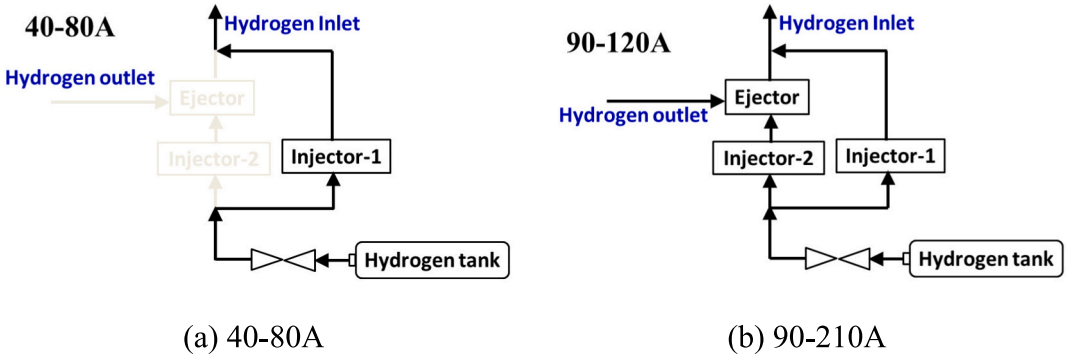

Fig. 18. Hydrogen supply sub-system.

control. Then the ejector will not work due to insufficient drive flow. Otherwise, it will further increase the St_a. Due to the lack of hydrogen circulation, the hydrogen utilization rate is low, and the hydrogen consumption is relatively high.

As the current gradually increases, the theoretical demand for the hydrogen flow rate will also increase. However, the opening of injector 1 is adjusted by the pressure PID and cannot continue to increase to satisfy the flow rate. When the flow rate passing through injector 1 cannot meet the demand, injector 2 will automatically open. As mentioned earlier, the opening of injector 2 is controlled by the flow rate. When St_a is lower than the set value of 1.5, injector 2 starts to operate. As shown in Fig. 16 (b), when the current increases to 90 A, the St_a reaches the above threshold. At this time, injector 2 opens under the action of PID, and the ejector begins to work (as shown in Fig. 18(b)). And then the implementation of hydrogen recycling significantly reduces the hydrogen consumption rate.

As the current further increases, the ejector remains in working condition. But as the anode operating pressure (Fig. 16(a)) further increases, the opening of injector 2 will gradually increase to increase the anode pressure, leading to a further increase in hydrogen consumption rate. Based on the above analysis, the hydrogen consumption rate and system efficiency curve shown in Fig. 17(b) were obtained. And 27.4 kW is the power P_{oe} (kW) at which the system efficiency reaches its maximum value, which will be used in energy management strategies (described in Section 2.3).

3.6. Dynamic variation of the operating condition under the NEDC cycle

The various operating conditions optimized under steady-state or stable conditions in the previous text can provide a reference for PEMFC operation regulation. However, in practice, FCVs face transient and complex driving environments. Then, it is difficult to maintain various PEMFC operating conditions stable. The vehicle powertrain also includes Li-ion batteries, in which case the energy management strategy has a significant impact on the vehicle's power and economy. This section is based on the two energy management strategies described in Section 2.3 and investigates the dynamic performance of the PEMFC itself and the vehicle under the NEDC cycle.

3.6.1. Operating condition variation

Fig. 19 illustrates the variation patterns of stoichiometric ratio, pressure, humidity, temperature, and load of the stack under the NEDC

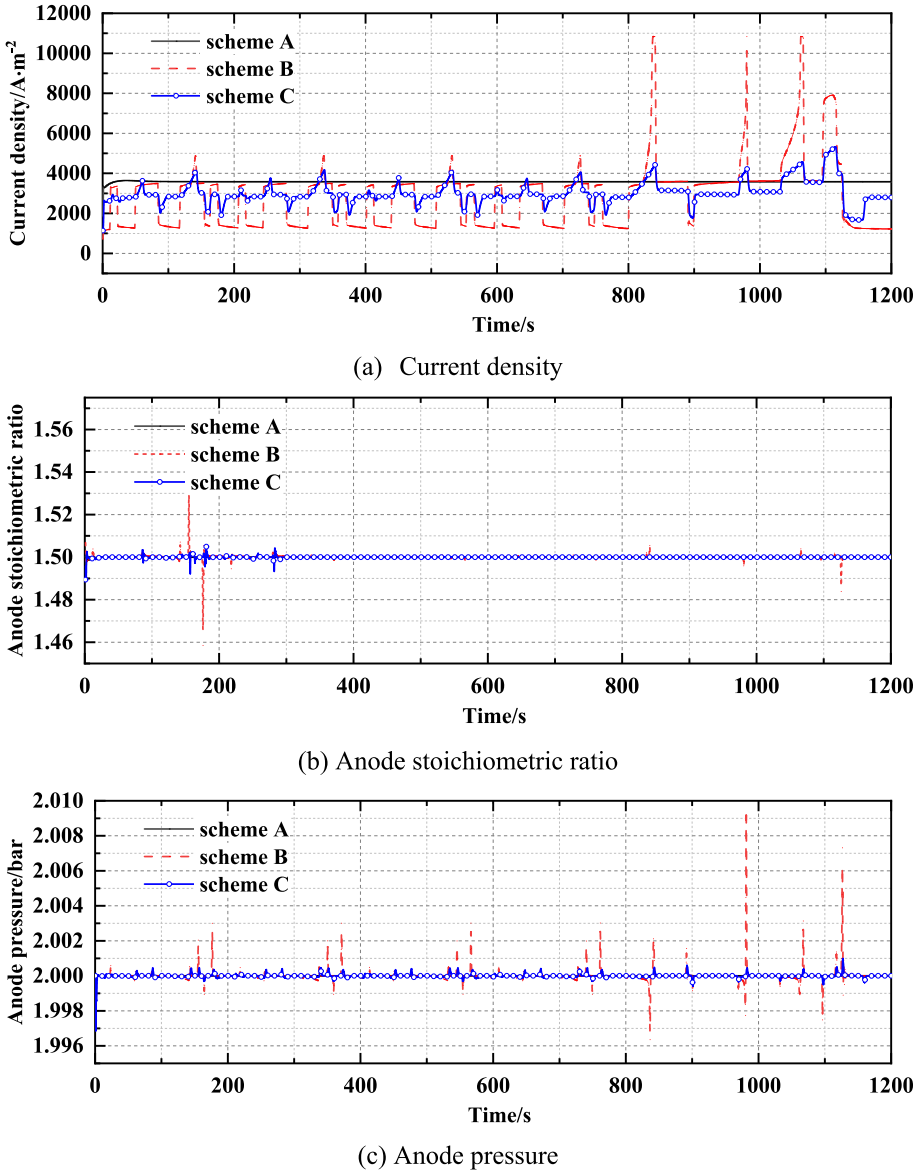

Fig. 19. Stack operating condition variation.

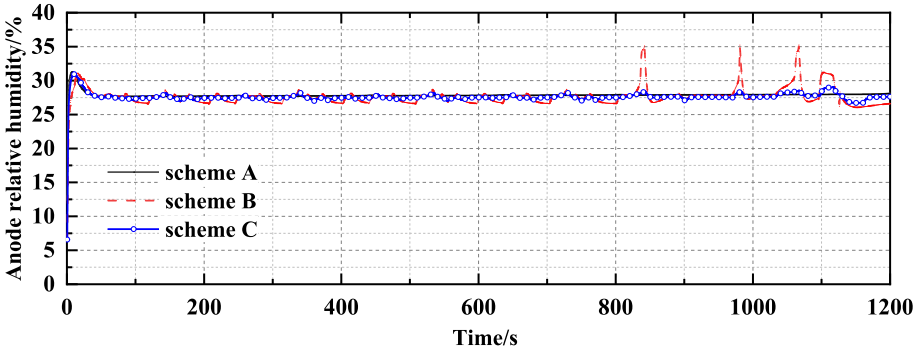

(d) Anode relative humidity

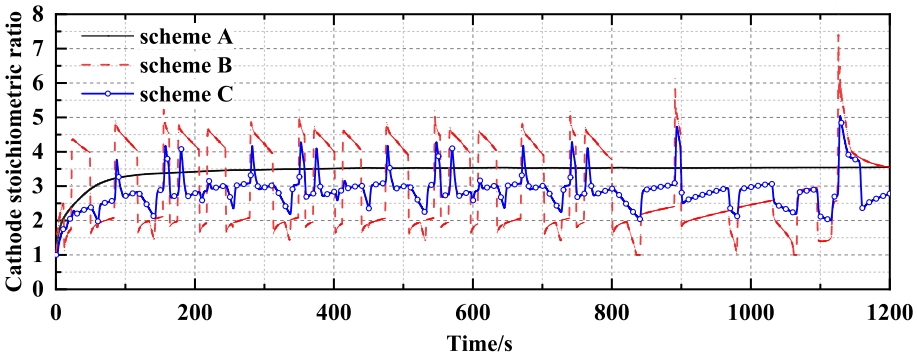

(e) Cathode stoichiometric ratio

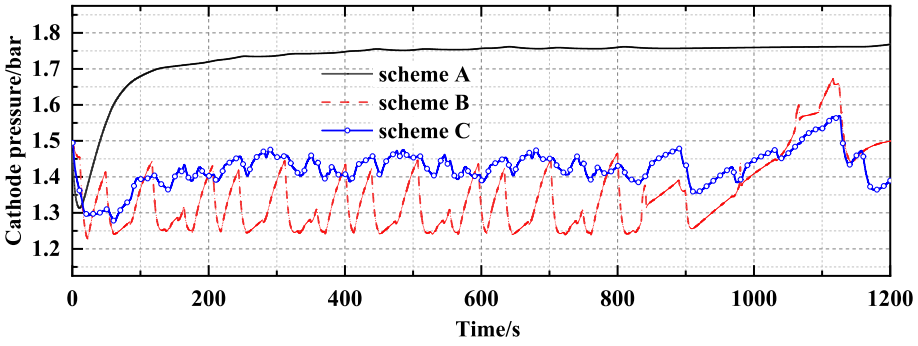

(f) Cathode pressure

Fig. 19. (*continued*).

cycle. Under different energy management strategies, the patterns of these parameters are significantly different. As depicted in Fig. 19(a), in scheme A, the average current density is maintained at 0.358 A·cm^{-2} (115 A), whereas in scheme B, the current density fluctuates between 0.119 and 1.084 A·cm^{-2}. Within a 1200s NEDC cycle, the period when the current reaches 115 A or above accounts for 19.5 %, and the rest are between 40 A and 115 A, which will result in energy savings. The fluctuation amplitude of the current density corresponding to scheme C EMS is very small. The current density range has decreased from 0.965 A·cm^{-2} in scheme B to 0.367 A·cm^{-2} in scheme C, which reflects the advantage of stable operation of the fuzzy control-based scheme.

The set values of the anode and cathode operating conditions follow the load current range and the experience in Section 3.5. On the anode side, the stoichiometric ratio is controlled at 1.5, and the anode pressure is maintained at 2.0 bar throughout the entire NEDC cycle. As shown in Figs. 19(b) and (c), under the hydrogen circulation configuration adopted in the current study (a hydrogen injection valve paired with an ejector), both parameters remain stable near their set values. The anode has no active humidification device, and its humidity level is determined by the hydrogen circulation system. Fig. 19(d) reveals that, after stabilization, the anode's relative humidity is maintained at approximately 27.7 %.

On the cathode side, the cathode pressure and flow rate are highly coupled. To reduce the complexity of the model, the open-loop control is employed in this study for both air compressor speed and back-pressure valve opening to minimize model complexity. Based on the steady results obtained in Section 3.5, the corresponding air compressor speed and back-pressure valve opening ratio are controlled in an open-loop manner for each load current, without feedback regulation. As illustrated in Figs. 19(e) and (f), in scheme A, with a constant current, the cathode stoichiometric ratio and pressure stabilize around 3.5 and 1.7 bar, respectively. In scheme B, with rapid current switching, the pressure fluctuates between 1.25 bar and 1.65 bar, and the stoichiometric ratio fluctuates between 2 and 5 for 90 % of the time. The cathode-side pressure remains lower than that of the anode side, which meets the preset requirements. At the moment of a sudden current jump, the cathode cannot provide enough air, and the stoichiometric ratio will drop sharply, and vice versa. In contrast, when introducing the fuzzy

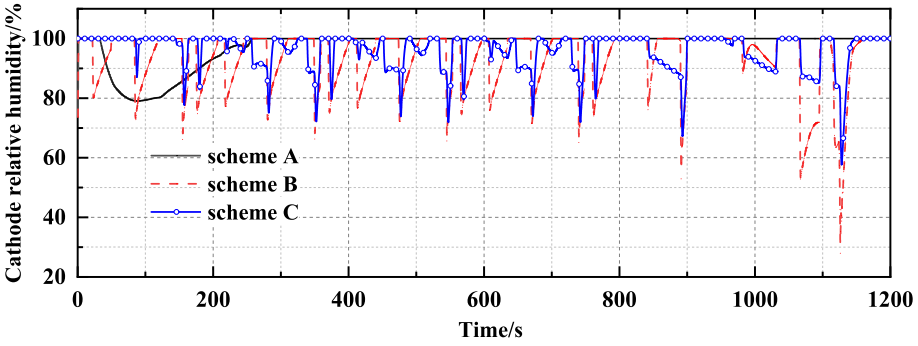

(g) Cathode relative humidity

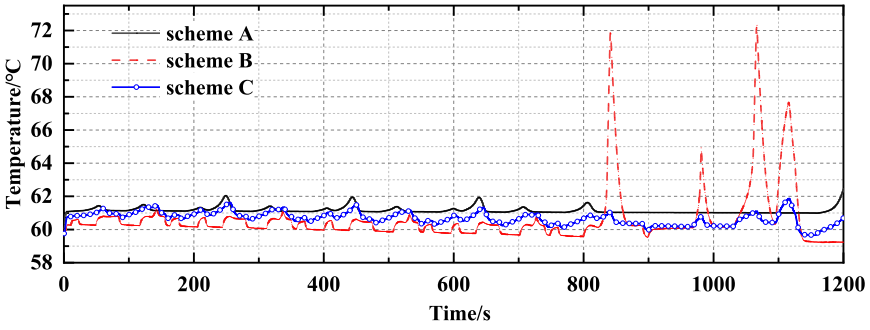

(h) Temperature

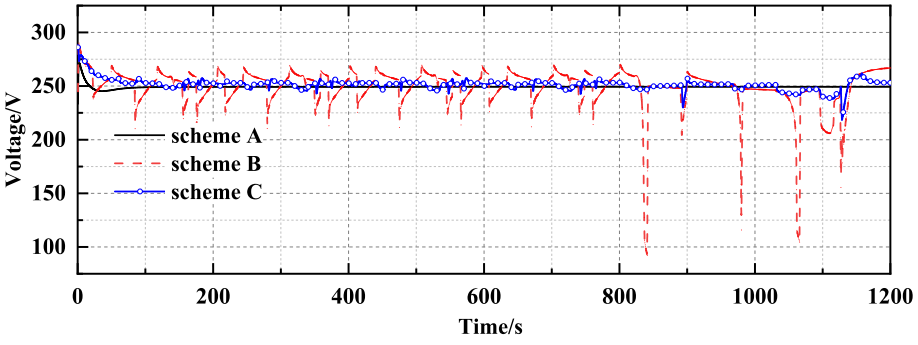

(i) Stack voltage

Fig. 19. (*continued*).

control-based EMS, it can be observed that the peak fluctuations in the scheme C EMS are weakened. The cathode stoichiometric ratio changes more smoothly, and the cathode pressure also exhibits this characteristic. Regarding relative humidity, as depicted in Fig. 19(g), in scheme A, 100 % humidification is maintained after stabilization. In scheme B, the humidity can be maintained at 100 % in most stages, except for the period when the stoichiometric ratio jumps suddenly, that is, the gas supply increases suddenly. Similarly, the scheme C EMS significantly mitigates the valley phenomenon in scheme B.

Figs. 19(h) and (i) shows the cell stack temperature and voltage variation during the NEDC cycle, respectively. For scheme A, the stack output voltage is unchanged (stable value 249 V, see Fig. 19(i)), and the fluctuation range of the stack temperature is small (see Fig. 19(h)). At this time, the change in vehicle speed causes a slight change in the heat dissipation of the thermal management system, which in turn causes small fluctuations (from 60.0 °C to 62.4 °C) of the stack temperature. For scheme B, due to changes in stack power, the stack temperature varies between 59.2 °C and 72.3 °C. Especially under high current, the PEMFC heat loss is large, and the stack temperature reaches the peak value. For example, when the current density reaches its maximum value of 1.084 A/cm^2, the stack temperature also peaks at 72.3 °C, accompanied by a low cathode stoichiometric ratio. Due to these factors, the stack voltage drops to its lowest value of 104.5 V. Nevertheless, it remains within a reasonable range. For scheme C, its temperature and voltage remain close to constant operating conditions, exhibiting very stable electrical and thermal performance. This is crucial for extending the lifespan of fuel cells and reflects its superiority over the power following strategy.

3.6.2. *Dynamic performance of the vehicle*

Fig. 20(a) shows the NEDC cycle speed and the actual vehicle speed under two energy management strategies. It can be seen that the hybrid system can meet the variable speed requirements of the vehicle and achieve accurate speed tracking. Fig. 20(b) shows the comparison of vehicle demand torque and motor output torque, which match well.

The motor torque depends on the vehicle's speed. Every time the vehicle switches between static, acceleration, constant speed, and deceleration, the driver makes corresponding actions, and finally, a step or sudden drop will appear on the motor torque curve. It is worth noting

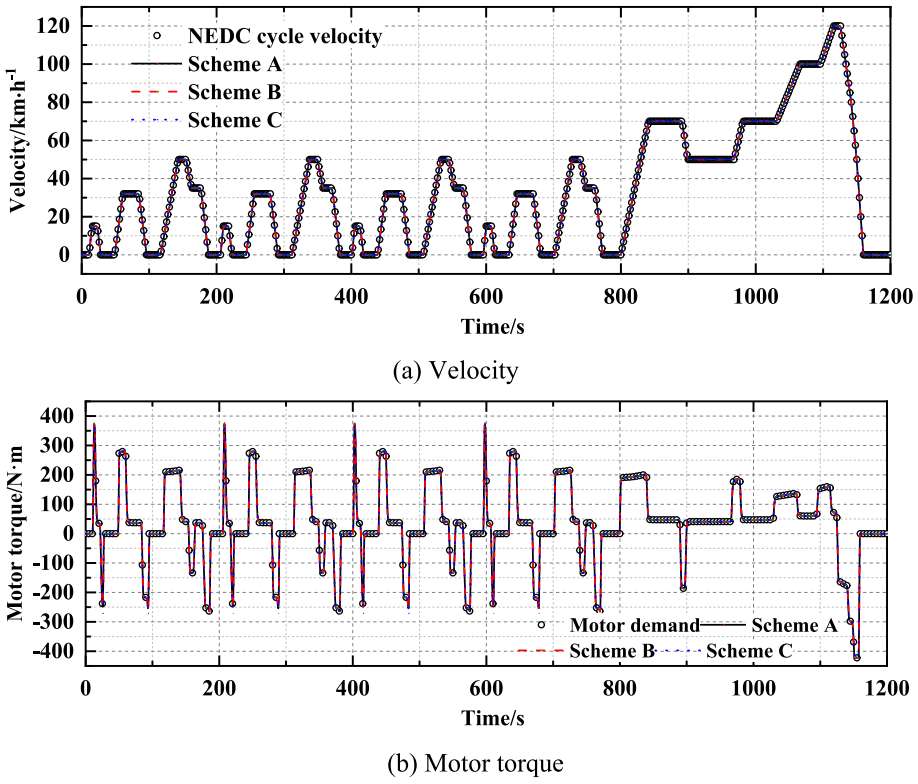

Fig. 20. Vehicle dynamic performance.

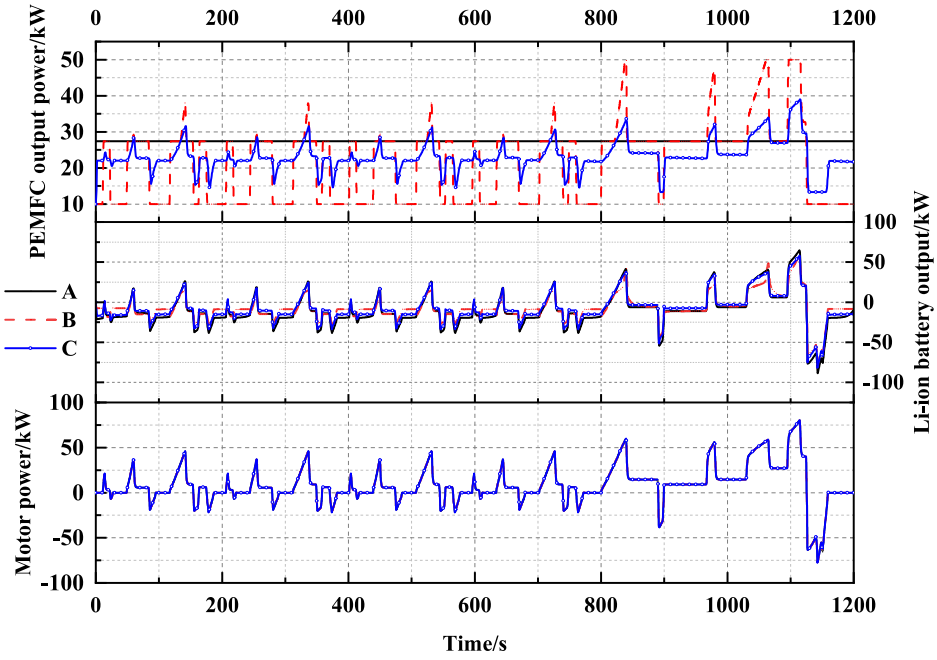

Fig. 21. Power distribution.

that when the vehicle decelerates, the motor torque is negative; that is, it generates power as a generator. The generated electric energy is transmitted to the high-voltage bus and then stored in the Li-ion battery through bidirectional DC-DC.

3.7. Fuel economy

In addition to meeting the dynamic performance, a good EMS should also be able to improve fuel economy. This section will analyze the fuel economy of three EMS.

Fig. 21 illustrates the variation in power output under the NEDC conditions. Under three energy management schemes, the driving motor's power remains consistent, dictated by the vehicle and driver models. However, there exists a discrepancy in the power distribution between the fuel cell and Li-ion battery.

In Scheme A, the fuel cell operates consistently at its optimal

efficiency point P_{oe} of 27.4 kW, without fluctuating in response to changes in the motor's power. Consequently, the Li-ion battery needs to absorb any excess power generated by PEMFC or supply any deficiencies. This leads to greater fluctuations in its power output compared to Scheme B, which can be observed in the middle graph in Fig. 21. Scheme C is between Schemes A and B. Overall, the fluctuations of P_{fc} from high to low are schemes B, C, and A. The fluctuations of P_{ba} from high to low are schemes A, C, and B.

Scheme A's merit lies in utilizing the Li-ion battery to smooth out power fluctuations, thereby enhancing the lifespan of the fuel cell stack. Conversely, the advantage of scheme B is that the fuel cell can work in the low power range for a long time, reducing hydrogen consumption. Its peak power requirements for Li-ion batteries are also reduced. The scheme C takes into account the advantages of both scheme A and B, and can better allocate the power between fuel cells and Li-ion battery. Due to the strong fault tolerance of fuzzy control and the role of sliding average filtering, the fluctuation of the output signal is significantly reduced, which can extend PEMFC lifespan.

It can be observed from Fig. 22(a) that the hydrogen consumption rate in scheme A is maintained at 0.399 $g{\cdot}s^{-1}$ after stabilization, while in scheme B, it fluctuates with power in the range of 0.123–1.196 $g{\cdot}s^{-1}$. As listed in Table 10, driving for about 10.93 km (NEDC cycle), schemes A, B, and C consume 478.3 g and 381.5 g, and 401.4 g of hydrogen, respectively. The overall hydrogen consumption of scheme A is 25.4 % and 19.2 % higher than that of scheme B and C, respectively. Corresponding to the hydrogen consumption, the average output power of the PEMFC stack in scheme A (27.4 kW) is also 27.4 % and 18.6 % higher than that in scheme B (21.5 kW) and C (23.1 kW), respectively. In scheme A, the fuel cell always works at 27.4 kW, while in scheme B, the duration of the fuel cell working at the optimal point of system efficiency (P_{oe} = 27.4 kW) and the lower limit point (10 kW) accounts for 45.4 % and 41.3 % respectively. Due to working at the lower limit (10 kW) for a long time, the hydrogen consumption rate in scheme B is small. The scheme C can also effectively reduce hydrogen consumption, but under the action of fuzzy control and sliding average filtering, to avoid severe power fluctuations caused by fuel cell operation at the lower limit power point, its hydrogen consumption slightly increases compared to the scheme B.

Fig. 22(b) shows the SOC (state of charge) change of the Li-ion battery, with an initial SOC of 60 %. At the end of the NEDC cycle, the SOC reached 93.0 %, 83.2 % and 84.4 % for schemes A, B, and C, respectively. The final SOC is consistent with hydrogen consumption. That means although scheme A consumes more hydrogen, more energy is injected into the Li-ion battery. When the vehicle is in the simulated suburban driving condition (period of 965 s ~ 1125 s), the speed increases gradually from 50 $km{\cdot}h^{-1}$ to 120 $km{\cdot}h^{-1}$. At this time, the motor needs a large power, and the Li-ion battery needs a large proportion of intervention to provide energy, leading to rapid SOC drops. For the rest of the period, the battery is generally charged, and only occasionally discharged when the vehicle accelerates.

Table 10
Energy comparison of scheme A and B.

	Scheme A	Scheme B	Scheme C
Total hydrogen consumtion/g	478.3	381.5	401.4
Average stack power/kW	27.4	21.5	23.1
Proportion of motor and battery /%	69.9	73.4	70.5

Fig. 23 shows the direction of the electric energy generated by the fuel cell. It can be seen that in scheme B, more power from the stack enters the motor, which is converted into mechanical energy to drive the vehicle forward. The proportion of energy transmitted to auxiliary machines and heat loss has decreased compared with scheme A. If the energy transferred to the battery for storage and the energy consumed by the motor are used as the energy for effective utilization, as listed in Table 10, the effective energy utilization rate of scheme A is 3.5 % and 0.6 % lower than that of scheme B and C, respectively. Therefore, this proves that the fuzzy control-based energy management strategy proposed in this paper can improve operating stability while also increasing energy utilization efficiency.

4. Conclusion

In the present study, a multi-level FCV system model is developed to analyze the vehicle dynamics and economic performance. Although this study focuses on a specific fuel cell stack and system architecture, the multi-level optimization method established in this study is also applicable to similar fuel cell hybrid power systems. This study has a significant impact on further improving the energy utilization efficiency of FCVs. The main findings of this study are as follows:

(1) ANOVA identified that current density, temperature, and cathode parameters (pressure, humidity, stoichiometry) are statistically significant voltage determinants, while anode humidity and stoichiometry showed negligible impacts. Therefore, more attention should be paid to the regulation and response of the air supply system during the load change process.
(2) The operating conditions of fuel cells have been optimized by combining machine learning and intelligent optimization algorithms to achieve maximum power density. The GPR model has

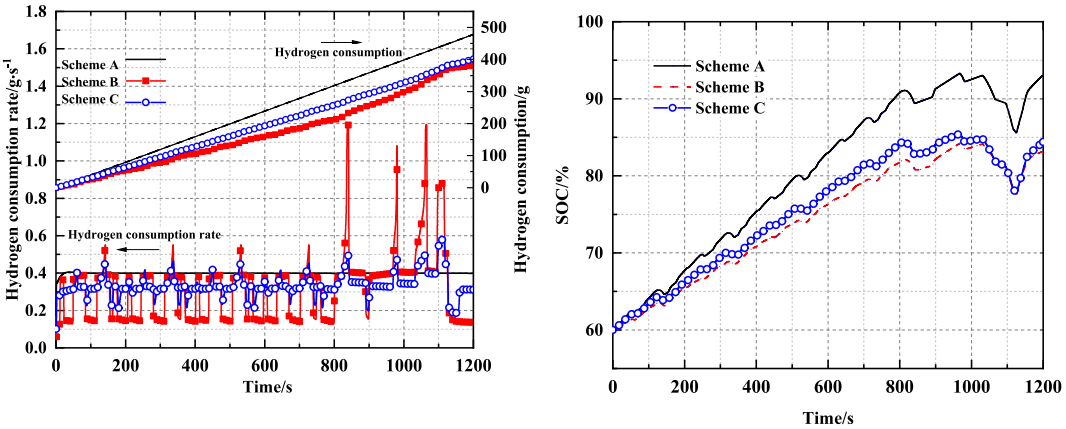

(a) Hydrogen consumption (b) SOC

Fig. 22. PEMFC and battery energy variation.

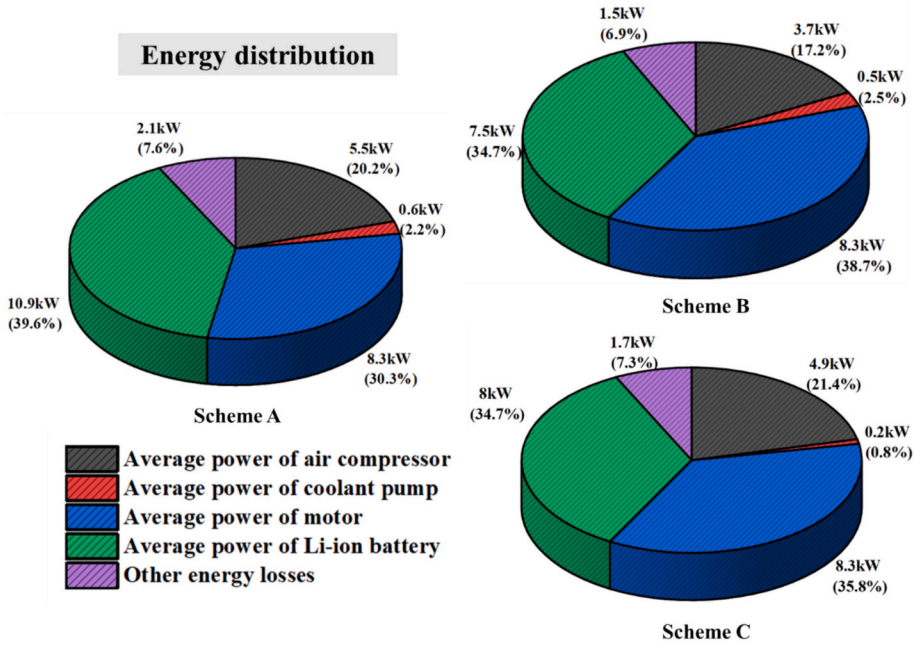

Fig. 23. Energy distribution.

the fastest prediction speed and prediction accuracy compared with other ML models (LR, SVR, and ANN). The optimization results of GA are better than PA, and the calculation speed is faster than PSO. This provides a reference for similar optimization research.

(3) The efficiency of the PEMFC system is not only related to parasitic power, but also depends on the hydrogen consumption rate. Under the hydrogen recirculation architecture of this study, the system efficiency reaches its peak (47.4 %) at a load current of 110 A, which corresponds to the lowest point of hydrogen consumption.

(4) The fuzzy control-based scheme is a compromise EMS between a constant power and a power following strategy. Although its energy utilization rate of 70.5 % is slightly lower than that of the power following strategy 73.4 %, it significantly reduces the frequency and amplitude of fuel cell power fluctuations, which is beneficial for extending the life of fuel cells. It is a promising energy management solution for FCVs.

5. Future research needed

It is worth pointing out that further in-depth researches are needed in the future, and to the authors' knowledge they can be indicated as follows: (1) The ML models of PEMFC are trained based on steady-state CFD model results. The systematic CFD analysis of transient PEMFC response should be carried out in the future. (2) Relevant system experiments need to be conducted to further validate the energy management strategy proposed in this study. (3) The multi-level research can be carried out on more system architectures, such as different hydrogen recirculation systems, and compare the differences in optimization results.

CRediT authorship contribution statement

Zhuo Zhang: Writing – original draft, Validation, Methodology, Investigation, Funding acquisition, Conceptualization. **Sai-Jie Cai:** Data curation. **Jun-Hong Cheng:** Formal analysis, Conceptualization. **Hao-Bo Guo:** Resources, Methodology. **Wen-Quan Tao:** Supervision, Funding acquisition.

Declaration of competing interest

The authors declare that they have no known competing financial interests or personal relationships that could have appeared to influence the work reported in this paper.

Acknowledgment

The study is supported by the Postdoctoral Fellowship Program and China Postdoctoral Science Foundation under Grant Numbers BX20240285M and 2025M770627, the Young Scientists Foundation of National Natural Science Foundation of China under Grant Number 52506103.

Appendix A. Appendix

The gas species conservation is governed by the following equation:

$$\begin{cases} \dfrac{dY_i}{dt} = \dfrac{1}{m}\left(\dfrac{dm_i}{dt} - Y_i\dfrac{dm}{dt}\right) \\ \dfrac{dm_i}{dt} = \sum_j q_j Y_{i,j} \\ \dfrac{dm}{dt} = \sum_i \dfrac{dm_i}{dt} \end{cases} \tag{A1}$$

where Y_i and m_i (kg) are mass fraction and mass of component i, respectively; q_j (kg·s^{-1}) is the mass flow rate into or out of port j; $Y_{i,j}$ is the mass fraction of component i in the mixed gas at port j. On the cathode side, i represents O_2 , N_2 , H_2O (water vapor); On the anode side, i represents represents H_2 and H_2O (water vapor).

According to the mass and energy conservation, as follows:

$$\sum_j q_j = \frac{dm}{dt} = \frac{d(\rho V)}{dt} \tag{A2}$$

$$\sum_j q_j h_j + \delta\dot{Q} = \frac{dU}{dt} = \frac{d(mh - pV)}{dt} \tag{A3}$$

where m (kg), ρ (kg·m^{-3}), U (J) and h(J·kg^{-1})is the total mass, density, internal energy and specific enthalpy of gas in the corresponding chamber; V (m^3) is the chamber volume; h_j (J·kg^{-1}) is the specific enthalpy of the gas at port j; $\delta\dot{Q}$(J) is the heat exchange. Expand Eqs. (A2) and (A3), as follows:

$$\sum_j q_j - \rho\frac{dV}{dt} - V\cdot\sum_i \left.\frac{\partial\rho}{\partial Y_i}\right|_{p,T,Y_{j\neq i}} \cdot\frac{dY_i}{dt} = V\cdot\left.\frac{\partial\rho}{\partial Y_i}\right|_{T,Y_j} \cdot\frac{dp}{dt} + V\cdot\left.\frac{\partial\rho}{\partial Y_i}\right|_{p,Y_j} \cdot\frac{dT}{dt} \tag{A4}$$

$$\sum_j q_j h_j + \delta\dot{Q} = h\sum_j q_j + \left(m\left.\frac{\partial h}{\partial p}\right|_{T,Y_j} - V\right)\frac{dp}{dt} + m\left.\frac{\partial h}{\partial p}\right|_{p,Y_j}\frac{dT}{dt} + m\sum_i \left.\frac{\partial h}{\partial p}\right|_{p,T,Y_{j\neq i}} \cdot\frac{dY_i}{dt} \tag{A5}$$

where p (Pa) and T (K) are the pressure and temperature of the gas in the chamber.

Then from the gas state equation:

$$\begin{cases} \left.\dfrac{\partial\rho}{\partial p}\right|_{T,Y_j} = \dfrac{\rho}{p} \\ \left.\dfrac{\partial\rho}{\partial p}\right|_{p,Y_j} = -\dfrac{\rho}{T} \\ \left.\dfrac{\partial\rho}{\partial p}\right|_{p,T,Y_{j\neq i}} = -\rho\dfrac{R_{g,i}}{R_g} \end{cases} \tag{A6}$$

$$\begin{cases} \left.\dfrac{\partial\rho}{\partial p}\right|_{T,Y_j} = 0 \\ \left.\dfrac{\partial\rho}{\partial p}\right|_{p,Y_j} = c_p \\ \left.\dfrac{\partial\rho}{\partial p}\right|_{p,T,Y_{j\neq i}} = -h_i \end{cases} \tag{A7}$$

The derivatives of pressure and temperature with time can be obtained by solving Eqs. (A4)–(A7) simultaneously.

Appendix B. Supplementary data

Supplementary data to this article can be found online at https://doi.org/10.1016/j.apenergy.2025.126678.

Data availability

Data will be made available on request.

References

[1] Hua Z, Gao W, Chi S, Wang X, Zheng J. Development status and challenges of high-pressure gaseous hydrogen storage vessels and cylinders in China. Renew Sustain Energy Rev 2025;214:115567.

[2] Rosner F, Papadias D, Brooks K, Yoro K, Ahluwalia R, Autrey T, et al. Green steel: design and cost analysis of hydrogen-based direct iron reduction. Energ Environ Sci 2023;16:4121–34.

[3] Makhsoos A, Kandidayeni M, Pollet BG, Boulon L. A perspective on increasing the efficiency of proton exchange membrane water electrolyzers– a review. Int J Hydrogen Energy 2023;48:15341–70.

[4] Zhang Z, Cai S-J, Li Z-D, Tao W-Q. Electrical and thermal performance analysis of PEMFC with coolant flow field under steady-state condition. Energy 2024;306:132288.

[5] Chen X, Long S, He L, Wang C, Chai F, Kong X, et al. Performance evaluation on thermodynamics-economy-environment of PEMFC vehicle power system under dynamic condition. Energ Conver Manage 2022;269:116082.

[6] Shojaeefard MH, Raeesi M. Dynamic analysis and performance improvement of a GDI engine and fuel cell under real driving conditions using machine learning technique. Int J Hydrogen Energy 2023;52:1115–26.

[7] Yang J, Chen L, Zhang B, Zhang H, Chen B, Wu X, et al. Remaining useful life prediction for vehicle-oriented PEMFCs based on organic gray neural network considering the influence of dual energy source synergy. Energy 2025;322:135578.
[8] Ahmadi P, Raeesi M, Changizian S, Teimouri A, Khoshnevisan A. Lifecycle assessment of diesel, diesel-electric and hydrogen fuel cell transit buses with fuel cell degradation and battery aging using machine learning techniques. Energy 2022;259.
[9] Olabi AG, Abdelkareem MA, Wilberforce T, Alami AH, Alkhalidi A, Hassan MM, et al. Strength, weakness, opportunities, and threats (SWOT) analysis of fuel cells in electric vehicles. Int J Hydrogen Energy 2023;48:23185–211.
[10] Zhang Z, Quan H-B, Cai S-J, Li Z-D, Tao W-Q. Design strategies for mainstream flow channels in large-area PEMFC: from typical units to large areas. Appl Energy 2025; 388:125628.
[11] Wang J, Jiang H, Chen G, Wang H, Lu L, Liu J, et al. Integration of multi-physics and machine learning-based surrogate modelling approaches for multi-objective optimization of deformed GDL of PEM fuel cells. Energy AI 2023;14:100261.
[12] Siddiqa S, Chang K, Naqvi SB, Azam M, Molla MM, Nguyen KH. AI-assisted proton exchange membrane (PEM) fuel cell performance prediction using CFD and data-driven surrogate models. Int Commun Heat Mass Transf 2024;156.
[13] Feng S, Huang W, Huang Z, Jian Q. Optimization of maximum power density output for proton exchange membrane fuel cell based on a data-driven surrogate model. Appl Energy 2022;317:119158.
[14] Zhou Y, Meng K, Liu W, Chen K, Chen W, Zhang N, et al. Multi-objective optimization of comprehensive performance enhancement for proton exchange membrane fuel cell based on machine learning. Renew Energy 2024;232:121126.
[15] Quan S, He H, Chen J, Zhang Z, Han R, Wang Y-X. Health-aware model predictive energy management for fuel cell electric vehicle based on hybrid modeling method. Energy 2023;278:127919.
[16] Lee S, Kim MS. Stack cooling system coupled with secondary heat pump in fuel cell electric vehicles. Energ Conver Manage 2023;284.
[17] Chen Z, Zuo W, Zhou K, Li Q, Huang Y, E J.. Multi-objective optimization of proton exchange membrane fuel cells by RSM and NSGA-II. Energ Conver Manage 2023: 277.
[18] Singh M, Mittal AP, Singh AK, Anand K. Heuristic power management of hybrid source electric vehicle based on PV-battery-PEMFC. Int J Hydrogen Energy 2024; 80:475–85.
[19] Aziz M, Trinh P-H, Hudaya C, Chung I-Y. Coordinated control strategy for hybrid multi-PEMFC/BESS in a shipboard power system. Electr Pow Syst Res 2025;243: 111495.
[20] Wu D, Li K, Gao Y, Yin C, Song Y, Yang X, et al. Experimental and modeling study on dynamic characteristics of a 65 kW dual-stack proton exchange membrane fuel cell system during start-up operation. J Power Sources 2021;481:229115.
[21] Salim RI, Noura H, Fardoun A. The use of LMS AMESim in the fault diagnosis of a commercial PEM fuel cell system. Adv Sci Technol Eng Syst J 2018;3:297–309.
[22] Chen K, Laghrouche S, Djerdir A. Performance analysis of PEM fuel cell in mobile application under real traffic and environmental conditions. Energ Conver Manage 2021;227.
[23] Atlam Ö, DÜNdar G.. A practical equivalent electrical circuit model for proton exchange membrane fuel cell (PEMFC) systems. Int J Hydrogen Energy 2021;46: 13230–9.
[24] Yang J, Chen L, Wu X, Deng P, Xue F, Xu X, et al. Remaining useful life prediction of vehicle-oriented PEMFCs based on seasonal trends and hybrid data-driven models under real-world traffic conditions. Renew Energy 2025;249:123193.
[25] Yuan X, Chen F, Xia Z, Zhuang L, Jiao K, Peng Z, et al. A novel feature susceptibility approach for a PEMFC control system based on an improved XGBoost-Boruta algorithm. Energy AI 2023:12.
[26] Zhang J, Liu B, Zhou Y, Huang X, Chen S, Xuan D. Hierarchical energy management strategy for fuel cell hybrid electric vehicles based on improved TD3 considering interior temperature comfort. Appl Therm Eng 2025;276:126965.
[27] Alhumade H, Rezk H, Louzazni M, Moujdin IA, Al-Shahrani S. Advanced energy management strategy of photovoltaic/PEMFC/lithium-ion batteries/ supercapacitors hybrid renewable power system using white shark optimizer. Sensors 2023;23:1534.
[28] Yang X, Tan P, Fang L, Zhuang C, Liu X, Xu H, et al. Dynamic performance and potential failure analysis of PEMFC system without external humidifier based on real vehicle testing. Int J Hydrogen Energy 2025;138:648–59.
[29] Li J, Liu J, Yang Q, Wang T, He H, Wang H, et al. Reinforcement learning based energy management for fuel cell hybrid electric vehicles: a comprehensive review on decision process reformulation and strategy implementation. Renew Sustain Energy Rev 2025;213:115450.
[30] Zhao ZL, Huang X, Wang YP, Du J, Ding TW, Zhao HH, et al. Simulation and experiment of power response control strategy for vehicle fuel cell. In: 46th annual conference of the IEEE-Industrial-Electronics-Society (IECON). Electr Network: Ieee; 2020. p. 5018–23.
[31] Zhang L, Li J, Li R, Yang X, Zhang T. Research on the hydrogen supply system of fuel cell for vehicle. J Eng Thermophys 2022;43:1444–59.
[32] Tanaka S, Nagumo K, Yamamoto M, Chiba H, Yoshida K, Okano R. Fuel cell system for Honda CLARITY fuel cell. eTransportation 2020;3:100046.
[33] Zhang Z, Shi J, Cheng X, Dai Y, Tao W. Numerical examination of high-pressure fuel injection in common rail injector based on hydro-mechanical model. Phys Fluids 2022;34:057114.
[34] Tan J, Hu H, Liu S, Chen C, Xuan D. Optimization of PEMFC system operating conditions based on neural network and PSO to achieve the best system performance. Int J Hydrogen Energy 2022;47:35790–809.
[35] Kuo-Chung T, Yu L. A test generation strategy for pairwise testing. In: IEEE transactions on software engineering. 28; 2002. p. 109–11.
[36] Chandran M, Palaniswamy K, Karthik Babu NB, Das O. A study of the influence of current ramp rate on the performance of polymer electrolyte membrane fuel cell. Sci Rep 2022;12:21888.
[37] Trinh H-A, Truong HVA, Pham MD, Do TC, Lee H-H, Ahn KK. Comprehensive control strategy and verification for PEM fuel cell/battery/supercapacitor hybrid power source. Int J Precis Eng Manuf 2022;10:421–36.
[38] Yan J, Rong Z, Wang Y. A model of PEMFC-battery system to evaluate inner operating status and energy consumption under different energy management strategies. Int J Hydrogen Energy 2022;47:3075–86.
[39] Zhang Z, Bai F, Quan HB, Yin RJ, Tao WQ. PEMFC output voltage prediction based on different machine learning regression models. In: 2022 5th international conference on energy, electrical and power engineering (CEEPE). IEEE; 2022. p. 401–6.
[40] Hammadi Y, Ryckelynck D, El-Bakkali A. Data-driven reduced bond graph for nonlinear multiphysics dynamic systems. Appl Math Comput 2021;409.
[41] Zhang Z, Wang Q-Y, Bai F, Chen L, Tao W-q. Performance simulation and key parameters in-plane distribution analysis of a commercial-size PEMFC. Energy 2023;263:125897.
[42] Xia Q, Zhang T, Sun Z, Gao Y. Design and optimization of thermal strategy to improve the thermal management of proton exchange membrane fuel cells. Appl Therm Eng 2023;222:119880.
[43] Li H, Xu B, Lu G, Du C, Huang N. Multi-objective optimization of PEM fuel cell by coupled significant variables recognition, surrogate models and a multi-objective genetic algorithm. Energ Conver Manage 2021;236:114063.
[44] O'Hayre R, Cha SW. Fuel cell fundamentals. 3rd ed. Canada: John Wiley & Sons, Inc., Hoboken, New Jersey; 2016.